Steady or Sudden: the 2008 Eruption of Okmok, Alaska

Daniel W. J. Lee[1], Terry Plank[1], Shuo Ding[1,2], Euan J. F. Mutch[3], Yves Moussallam[1], Jamshid Moshrefzadeh[4,5], Nathan Graham[4], Jessica Larsen[4]

[1]Lamont Doherty Earth Observatory, Columbia University, Palisades, NY, USA
[2]Department of Geological Sciences, University of Florida, Gainesville, FL, USA
[3]Earth Observatory of Singapore, Nanyang Technological University, Singapore
[4]Geophysical Institute, University of Alaska Fairbanks, Fairbanks, AK, USA
[5]Alaska Division of Geological and Geophysical Surveys, Fairbanks, AK, USA

Abstract

The 2008 eruption of Okmok (OK08) had among the shortest run-ups for an arc volcano (~5 hours of heightened seismicity), yet also experienced over a decade of inflation since its prior eruption in 1997. Was OK08 driven by steady inflation or a sudden diking event? To answer this question, we investigated OK08 melt inclusions and olivines to constrain the depth and timing of magmatic events. We homogenized olivine-hosted melt inclusions and found CO_2 concentrations up to 1800 ppm, providing new evidence for a mid-crustal magma storage region (~15 km) beneath Okmok that aligns closely with the deepest earthquakes found during the five-hour precursory seismicity. These high CO_2 melt inclusions are hosted in olivines that are unzoned in Fe-Mg, constraining residence in host magma to less than a day. Hence, the precursory seismicity was magmatic, and the eruption expelled crystals that could have risen five hours prior to eruption. Fe-Mg diffusion timescales and crystal depths also show magma movement beneath Okmok during its inter-eruptive period, with three dominant reservoirs at depths from 15 to 1 km. Mixing took place at least five years prior to eruption with an increasing number of olivines reflecting mixing timescales in early 2008. This magmatic ramp-up aligns with the shifting of the deformation source and proposed tensile failure of the reservoir in the months prior to eruption. The occurrence of

both steady and sudden processes culminated in OK08. Sudden explosive eruptions could be a consequence of a magmatic system 'primed' by years of slow magma input.

1. Introduction

Volcanic eruptions are often preceded by escalating levels of unrest, known as run-up (Passarelli & Brodsky, 2012). Identifying run-up is critical to our ability to forecast eruptions and issue effective warnings (Pesicek et al., 2018). Extremely short run-ups are particularly problematic for providing timely warnings. When such eruptions occur, it is critical to analyze in hindsight the pre-eruptive geophysical signals to better prepare for future eruptions. The 2008 eruption of Okmok volcano (OK08), Alaska, is an example of an eruption with an extremely short run-up, with a mere five hours of heightened seismicity preceding the VEI 4 eruption (Johnson et al., 2010; Larsen et al., 2009; Fig 1a.). In the compilation of Passarelli and Brodsky (2012), OK08 is the arc volcano with the shortest run-up globally. Since then, other eruptions have been identified with no apparent run-up (e.g., Pavlof 2016; Pesicek et al., 2018). The precursory behavior of OK08 was in stark contrast to the inter-eruptive period (1997–2008), when there was episodic inflation for over a decade but with little seismicity (Freymueller & Kaufman, 2010; Johnson et al., 2010; Lu et al., 2010; Power et al., 2019; Fig. 1b). Approximately two-to-three months before the eruption, there was a distinct shift in the long-term deformation source or change in source geometry (Freymueller & Kaufman, 2010).

Recent studies by Albright et al. (2019) and Garza-Girón et al. (2023) propose two opposing interpretations to the trigger of OK08 based on geodetic and seismic data, respectively. Albright et al. (2019) propose Okmok reached critical tensile failure in the months prior to eruption, primed by years of inflation. We refer to this run-up as slow and steady. On the other hand, Garza-Girón et al. (2023)'s used their enhanced earthquake catalogue to suggest a deep and

rapid trigger initiating 5 hours before eruption, linked to the opening of a planar feature that extended to the maximum depth of seismicity of ~15 km. This view implicates a sudden run-up to eruption.

Okmok thus displayed unrest over many timescales: from years of episodic inflation, to months of change in the inflation source and stress state, to hours in an earthquake swarm that immediately preceded eruption. Such protracted episodes and manifestations of unrest have been termed "ultimate," "proximal," and "immediate" by Putirka (2017), and have obvious implications for successful eruption forecasting. Seismicity and deformation are non-unique to specific magmatic processes (McNutt & Roman, 2015; Wauthier et al., 2016), and understanding the warning signs to eruption requires an understanding of the magmatic system – its distribution within the crust, the timing of magma ascent and storage, and factors that control magma buoyancy, viscosity, volatile concentration and composition. Such information can only be provided by studying eruptive products, as they encode in their chemical composition such vital information. Specifically, petrological tools such as diffusion chronometry and solubility barometry can provide a timeseries of storage depth and composition that can then be mapped to geophysical timeseries (Kahl et al., 2022; Lynn et al., 2024; Rasmussen et al., 2018).

To explore this well-posed example of steady vs. sudden run-up, we examine here the earliest erupted products of OK08 (Larsen et al., 2013) using 1) olivine diffusion chronometry to provide the timing of magma mixing, 2) volatile solubility to provide the depth of magma residence leading up to OK08 and 3) major and trace element compositions of whole rock, glass and mineral phases to provide constraints on the different magma bodies tapped. With this dataset, we address the following fundamental questions. Is the precursory seismicity related to magma movement? Can we associate syn-eruptive and inter-eruptive geophysical observations with magmatic events?

2. Background

On July 12, 2008, Okmok volcano produced a 16 km eruptive column and extensive tephra fall-out over a period of 4 hours (Larsen et al., 2009, 2015; Unema et al., 2016). Weak ash emissions continued from multiple vents until activity ceased on August 19, 2008. In this study we focus on the July 12 phase of the eruption, which produced scoria fall units deposited inside and outside the caldera (0.048 km^3 DRE erupted volume and 9.85 x 10^6 kg/s discharge rate; Larsen et al., 2015; Unema et al., 2016).

OK08 had several unique features. First, the vent shifted away from Cone A, the eruption site over the past two centuries, to form a new cone, Ahmanilix (Larsen et al., 2015; Fig. 1a). Second, OK08 (VEI 4) was the most explosive eruption since Okmok-II, the caldera-forming eruption in BCE43 (Larsen et al., 2013). Third, the geochemistry of the newly erupted products was diverse, spanning from basaltic to andesitic compositions (Larsen et al., 2013). The first ash erupted during OK08 contained a unique population of primitive olivine-hosted melt inclusions (MIs) that were found in neither the 1997 scoria (Zimmer et al., 2010) nor the lapilli/bomb samples of the main July 12 phase (described as scoria in Larsen et al., 2013). Additionally, the whole rock composition of the main July 12 phase was more evolved (55.5 wt.% SiO_2) than the previous 1997 and 1958 eruptions (52 wt.% SiO_2; Finney et al., 2008; Larsen et al., 2013). Finally, the temporal pattern of precursory seismicity, predominantly volcano-tectonic (Garza-Giron et al., 2023), did not progress from shallow to deep, unlike the "top-down" behavior of other Aleutian volcanoes (Roman & Cashman, 2018).

The current model for OK08 is that the five-hour seismicity was related to dike intrusion from the main storage region (at ~3.4 km below the surface, the depth of the long term deformation source, Lu et al., 2010; Wang et al., 2021) to a shallower, older and chemically evolved body

beneath Cone D (Larsen et al., 2013; Ohlendorf et al., 2014; Miller et al., 2020 Fig. 1a). The expulsion of resident magma was supported by the volume change during the eruption (0.14±0.01 km^3), ~3x greater than the 1997-2008 inflation (~0.05 km^3) (Lu & Dzurisin, 2010; Fig. 1b). A shallow sill at ~1.4 km was later identified in the post-2008 inflation (Xue et al., 2020). Seismic tomography studies show a more complex magmatic architecture, including a deeper sill at 2 to 6 km and a deeper storage region up to 10 km depth (Kasatkina et al., 2022; Miller et al., 2020; Ohlendorf et al., 2014). Finally, Walwer et al. (2019) proposed that oscillatory deformation following inflation events during the inter-eruptive period could represent a hydraulic connection between two shallow reservoirs. These proposed interactions between deep and shallow magma reservoirs in the decade prior to OK08 motivates this petrological study to constrain the timing and depth of magma mixing beneath Okmok.

3. Materials and Methods

Critical to this study was the distal collection of ash samples erupted in the first few hours of OK08, as this material contained crystals and melt not present later in the July 12 main phase (Larsen et al., 2013). We focus here on the ash sample 08LKOK001 (described in Larsen et al., 2013) and collected on a boat by rancher Lonnie Kennedy while evacuating from Umnak Island. Loose olivine crystals were picked and examined for MIs that were glassy, free of crystals, fully enclosed in olivine, and without cracks, following Rose-Koga et al. (2021) (Fig. 2b and Supplementary Information, SI, -1). We also selected free-standing matrix glasses (MGs) that exhibited minimal microlite growth. For diffusion chronometry, we selected euhedral olivines with adhered matrix glass as an indication of the rim. See SI-1 to SI-7 for detailed methods and Supplementary Dataset, SD, -1 and-2 for all data.

3.1 Melt inclusions, matrix glass and bulk ash analyses

To account for CO_2 in MIs that contained vapor bubbles, we homogenized MIs using the piston cylinder method of Rasmussen et al. (2020) at the Lamont-Doherty Earth Observatory (LDEO) (SI-2 and Fig. 2b and 2c). Subsequently, homogenized, bubble-free (untreated) and bubble-bearing (untreated) MIs, and free-standing MGs were doubly polished (Fig. 2c) to quantify H_2O and CO_2 concentrations using a Thermo-Nicolet iN10 Fourier Transform Infrared Spectrometer (FTIR) at LDEO. FTIR spectra (Fig. 2a) were processed using the PyIRoGlass package to account for baseline uncertainties and compositional effects on absorption coefficients (Shi et al., 2024; SI-3). Major elements, sulfur and chlorine in MIs and MGs, and major elements of host olivines were measured on a Cameca SX-5 electron probe micro analyzer (EPMA) at the American Museum of Natural History (AMNH) (SI-4). We also analyzed the major elements of 11 MGs adhered to the olivine. A subset of the MIs and MGs were further analyzed for trace elements on a laser ablation inductively coupled plasma mass spectrometer (LA-ICP-MS) at Cornell University (SI-5). MIs were corrected for post-entrapment modifications (Danyushevsky et al., 2000) using MIMiC (Rasmussen et al., 2020) with Fe^{3+}/Fe^{T} fixed at 0.20 (as for 1997 scoria, Andrys, 2023) and using the Fe-Mg (ol/liq) partition coefficient expression in Toplis (2005). The bulk geochemical composition of the initial ash sample, 08LKOK001, was carried out following $LiBO_2$ flux fusion using an ICP-OES at LDEO (SI-6).

3.2 Diffusion chronometry

Olivines were analyzed by backscatter electron imaging using a JEOL JCM-7000 NeoScope Scanning Electron Microscope at LDEO to identify different zonation patterns. Chemical profiles were measured using a JEOL-8530F EPMA at the University of Alaska,

Fairbanks Advanced Instrumentation Laboratory and at the AMNH with a high sensitivity analytical routine for major and trace element profiles (SI-4). Orientations were later verified using electron backscattering diffraction on a Scanning Electron Microscope JSM-7800F at the Earth Observatory of Singapore. Corrections were made to the diffusivities to account for diffusive anisotropy in olivine (Costa & Dungan, 2005).

We modeled olivine Fe-Mg profiles using a 1-D finite difference model (see SI-7 for model design, errors and parameters). Additionally, we also performed forward 1-D and 3-D finite difference modeling to estimate the maximum timescale for which unzoned olivine crystals may reside in non-equilibrium melt and the timescales for the loss of olivine core compositions, respectively.

4. Whole rock, melt inclusions and glass chemistry

4.1 Homogenization experiments

After the homogenization experiments, 26 MIs were glassy and free from other phases (Fig. 2b), while 6 MIs crystallized small sulfide globules (due to the lowering of fO_2 during the experiment; (Ding et al., 2025; Taracsák et al., 2023). Five MIs also experienced decrepitation during the experiments, indicated by an excess of K_2O (KBr is used as a cushioning matrix). These MI were corrected using the K_2O–SiO_2 trend defined by the rest of the MIs and are distinguished by a different symbol in the figures (SI-8). CO_2 concentrations in the MIs are not affected significantly by these processes, as experimental homogenization can lead to many-fold increases in CO_2, and decrepitated MIs can also retain high volatile concentrations (Ding et al., 2025).

4.2 Major and trace elements

The bulk ash from the initial phase of the eruption is more mafic (52.5 wt.% SiO_2) than the main July 12 phase of the eruption (55 wt.% SiO_2) (SD-1). The initial ash is also significantly richer in phenocrysts (33% crystals, SI-9) compared to the largely aphyric main phase scoria (Larsen et al., 2013). Compositions of MIs and MGs analyzed in this study overlap well with those in Larsen et al. (2013) (Fig. 3a). The offset in SiO_2 between the homogenized MIs and untreated MIs studied here is a function of selecting mostly bubble-free MIs for the untreated population, and not related to the homogenization procedure. The bubble-bearing MIs from the initial ash contain low SiO_2 (<50 wt. %) compositions not observed in the bubble-free MI population, nor in any of the later-erupted products, nor in 1997 MIs (Larsen et al., 2013; Zimmer, et al., 2010). Thus, olivines with unique, primitive melts erupted in early OK08 only. The large range in SiO_2 observed in the early MGs reported by Larsen et al. (2013) is due in part to differences between free-standing (55–57 wt. %) and olivine-adjacent MGs (51–54 wt. %). The more mafic melt surrounding olivine grains is not caused by olivine dissolution or boundary layer effects, as incompatible elements such as Ca and Cl do not deviate from the trend defined by all other MIs and MG (Fig. 3a and SI-10; Shea et al., 2022). Thus, the olivine-adjacent MG appears to be a separate liquid that did not mix with the resident, more silicic melt.

Figure 4 and S11 show the trace element variations in MIs, MGs and WRs erupted from Okmok since the last caldera-forming eruption in BCE 43. All compositions define a coherent liquid line of descent (LLD) in V, with a clear kink when magnetite appears along the cotectic (and strongly partitions V). The MIs from the initial ash were entrapped before magnetite crystallization, while the free-standing MGs and 2008 main July 12 phase WR formed after magnetite crystallization (Fig. 4b). Cr is singled out by Larsen et al. (2013) as a distinguishing feature of OK08 relative to the adjacent Cone B magmas from the 1817 eruption. Olivine host

Forsterite (Fo) content decreases with decreasing Cr in the MI, consistent with co-crystallization of olivine, clinopyroxene and Cr-spinel. The low SiO_2 MIs have elevated Cr contents above any of the post-caldera WRs (Fig. 4a). For Sc, the MIs and MGs fall within the scatter of WRs which rules out melting of pyroxene-rich lithology to explain the low SiO_2 and high CaO MIs (Larsen et al., 2013). Instead, these low SiO_2 - high CaO MIs have elevated Al_2O_3 and positive Eu anomalies, consistent with plagioclase dissolution. Despite the wide variety in major element compositions, all OK08 MI, MG and WR fall on the same Th vs. Nb trend, indicating a common parentage (Fig. 4e).

4.3 Volatiles and saturation pressures

Water concentrations span between 0.77–2.4 wt.% for homogenized MIs and 0.92 – 1.75 wt.% for bubble-free MIs, within the range found previously in the same sample (Larsen et al., (2013), with the exception of one MI with an anomalously high concentration of 3.6 wt.% H_2O). The free-standing MGs record lower water contents, 0.5–1.02 wt.% (Fig. 3b).

Homogenized MIs that crystallized sulfide have S concentrations between 1000–1200 ppm, consistent with the predicted concentration at sulfide saturation (Smythe et al., 2017). Samples without sulfide have S concentrations of 118–1443 ppm for bubble-bearing MIs and 179–532 ppm for bubble-free MIs. S concentrations are below detection limit (~90 ppm) in MGs. The maximum S concentration in OK08 MIs (1443 ppm) is similar to that from other Okmok eruptions (~1300 and ~1600 ppm in 1997 and Okmok II, respectively; Zimmer et al., 2010, Peccia et al., 2023).

The majority of MIs and all MG have CO_2 below detection limit (< 100 ppm, calculated using equations in Shi et al. (2024) and dependent on sample thickness). Only 11 of the 32 homogenized MIs have detectable CO_2, which ranges from 150 to 1772 ppm (Fig. 3b). All these

values are substantially higher than the maximum of 49 ppm CO_2 found in untreated samples (Larsen et al., 2013), confirming the well-known importance of shrinkage bubbles in quantifying the total inventory of CO_2 hosted within MIs (Hartley et al., 2014; Moore et al., 2015). The very low S (<532 ppm), CO_2 concentrations (detection limit, <62 ppm) and evolved compositions in bubble-free MIs (>52 wt.% SiO_2) also calls into question the approach of several studies that only focus on bubble-free MIs (e.g., Hélène et al., 2023; Hlinka et al., 2021). While avoiding the bubble problem, study of such MIs may bias results to the shallow pressures and more evolved compositions.

In order to calculate the vapor-saturation pressures of the MIs, we use the python package VESIcal (Iacovino et al., 2021; Wieser et al., 2022) with the solubility model MagmaSat (Ghiorso & Gualda, 2015), as it covers the range of silica observed in MIs and MGs from OK08 (46–57 wt.% SiO_2, Fig. S12). MIs record saturation pressures up to 409 MPa (~15 km), with most recording less than 100 MPa (~4 km; Fig. 3b; using the Okmok-specific density model in Rasmussen et al. (2022) to iteratively convert pressures to depths).

As the majority of the MIs analyzed here have CO_2 below detection limit and could have experienced diffusive H_2O loss (Barth et al., 2019; Portnyagin et al., 2008) (Fig. 3b and S13), their saturation pressures place them within a shallow storage region (~1–2 km), representing their last depth of re-equilibration. On the other hand, the MI that records the highest pressure (~15 km) provides the first direct evidence for magmatic inputs from the mid-crust feeding Okmok eruptions.

5. Olivine populations and timescales

Olivine phenocrysts range in composition from Fo_{72} to Fo_{86} (Fig. 5a), with both zoned and unzoned populations. The decoupling of the zonation profiles across various elements suggests chemical diffusion rather than growth zoning (SI-14). Interestingly, olivine rims show limited variation ($Fo_{77–82}$), while cores show the entire range of measured Fo ($Fo_{72–86}$), reflecting equilibration with the wide range of OK08 liquids. Fo_{86} cores are in equilibrium with the most primitive MIs; Fo_{72} cores are in equilibrium with the free-standing MG and main scoria WR.

To further characterize the population of olivine crystals from this eruption, we evaluate the backscatter electron (BSE) images of 72 randomly selected crystals (Fig. 5b). In this way, we reduce bias from crystals analyzed for diffusion chronometry, where unbroken, zoned crystals were preferentially selected. We categorize these diverse olivines into four populations. P_1, sharp profile (Fo plateaus < 100 μm from rim); P_2, shoulder profile; P_3, long profile (Fo plateaus > 100 μm from rim). P_4, unzoned (SI-15).

5.1 Crystal timescales

Most olivine chemical profiles do not display a distinct sigmoidal shape, and thus initial conditions were difficult to determine. Some profiles show enrichment in P, often associated with a rapid growth boundary (Milman-Barris et al., 2008), allowing assignment of an initial step in the compositional profile. In cases where we were unable to distinguish a step or obtain an acceptable fit, we modeled two timescales: one initially homogenous and the other with a step profile (as in Rasmussen et al., 2018), and reported the timescale with the lower error. A recent study by Shea et al. (2023) finds that melt-bearing experiments show enhanced diffusivities in olivine, ~ 10x that in melt-free experiments of DC07 (Dohmen & Chakraborty, 2007). We report in SD-1 results using both the Shea et al. and DC07 diffusivities.

Crystal timescales, using DC07 diffusivities, span from weeks to five years before the eruption (Fig. 5c and 6). We binned the timescales into three general populations: 1) weeks (Fig. 6a), 2) months (Fig. 6b) and 3) years (Fig. 6c). These bins also help to assign approximate timescales to the BSE profiles: P_1 (sharp) profiles reflect magma mixing within weeks to months before the eruption, while P_3 (long) profiles experienced magma mixing more than a year prior to eruption.

With timescales of years before OK08, diffusion may reach olivine cores and thereby confound efforts to use the core composition as the initial condition. Using the measured core composition in these cases would underestimate the true time (Shea et al., 2015; Mourey et al., 2023). To test the extent of loss of initial core composition, we used the 3-D finite difference model by Shea et al. (2015) for an initially homogenous Fo_{72} crystal surrounded by magma in equilibrium with Fo_{80} with crystal diameters of 500 μm (mean crystal size in this eruption) and 1 mm (max; Fig. 7f). We extracted profiles along the [001] axis through the core of the crystal along the [100]-[001] plane, which is the most ideal transect for 1-D profiles (Shea et al., 2015). For OK08, 500 μm crystals would have lost ~2 mol % Fo after a year of diffusion while 1 mm crystals would still retain initial core compositions (Fig. 7f). Evidence for loss of core compositions is shown in Fig. 5c, where the longest (red) timescales do not have end-member core compositions (Fo_{72} or Fo_{86}). Thus, the Fo diffusion clock may lose resolution after a year and not capture older timescales for crystals with longer residence in the Okmok system (Mourey et al., 2023).

Some olivines appear unzoned in their EPMA profiles (Fig. 7d and S10), which generally start within 5 to 10 μm from the rim (Barth et al., 2024; Lynn et al., 2017). Higher resolution BSE images of some of "unzoned" crystals do show a change in greyscale (Fe/Mg) within 10 μm of the rim (SI-16), possibly representing quench overgrowths similar to those observed in Rasmussen et

al. (2018). However, if those changes in greyscale represent diffusion, we can estimate the maximum time the crystal could reside in a non-equilibrium magma and remain "unzoned" in EPMA profiles. We use a forward 1-D finite difference model with DC07 diffusivities to obtain expected profiles along the [001] and [100] axes (diffusively fast and slow, respectively). We modeled an initially homogenous end-member crystal, Fo_{86}, mixing with a magma in equilibrium with the mean rim composition Fo_{80} (Fig. 7d) and consider both axes, as the unzoned crystals were not oriented. Assuming no growth or resorption, this model crystal would show no detectable Fo change beyond 5 microns from the crystal rim within two to three days for the [100] axis and less than a day for the [001] axis. Some of the unzoned olivines were experimentally treated to homogenize their MIs and may have experienced some resorption or diffusion. However, given the distinct euhedral faces (Fig. 7a, b and 7c) and short laboratory heating times (minutes), any resorption and diffusion should not significantly alter the observed profiles. Thus, we can conclude that unzoned crystals that are not in equilibrium with the host melt have a maximum residence time of less than a day.

6. **Discussion**

6.1 Diversity of melt inclusions and architecture of the Okmok system

The OK08 tephra contains a diversity of MIs and olivines that are both more primitive and more evolved in composition than the products of the last eruption in 1997 (Fig. 3a). To explain these diverse compositions, we propose at least three distinct reservoirs were tapped during OK08. The chemical composition and depth of the magma in these reservoirs is constrained by our MI-MG analyses. The first reservoir is what we consider the main reservoir (R_m), coincident with the long-term inflation source beneath Okmok. The composition of R_m is similar in bulk composition to the magmas erupted from Cone A in 1958 and 1997 (52–53 wt.% SiO_2, aphyric). The Cone A

WRs are in equilibrium with $Fo_{76–82}$ (assuming Fe^{3+}/Fe^{T} of 0.2 and $K_{D\ ol/melt}$ = 0.3, Fig. 5a), which overlaps well with the olivine rims in OK08. The MG surrounding the OK08 olivines is also similar in composition to the 1997 WR (Fig. 3, 4). This suggests tapping of the same storage region in 1997 and 2008 (Finney et al., 2008; Larsen et al., 2013; Zimmer et al., 2010). Additionally, $Fo_{79–82}$ olivines host MIs with Cr contents that overlap with the 1958, 1997 and historical Cone A and Cone D WRs (Fig. 4a). These intermediate compositions (51–53 wt.% SiO_2) are not created by the mixing of the primitive and evolved endmembers, as constrained by the kinked V-SiO_2 LLD (Fig. 4b, where the 1997 WR plots at the maximum V). Additionally, given that the inflation between 1992–2008 remained consistent in depth and location (Fournier et al., 2009; Lu et al., 2005; Lu & Dzurisin, 2010), except for the 3–4 months prior to OK08 (Freymueller & Kaufman, 2010), this liquid in equilibrium with ~$Fo_{76–82}$ likely represents the composition of Okmok's long term main storage region at ~3 km (Fig. 8d). The MG surrounding OK08 olivines represents the R_m liquid. We note that the composition of the initial ash (52.5 wt.% SiO_2 and Fo_{80} equilibrium olivine) is also consistent with derivation from R_m and implicates its early tapping.

Although R_m is important to the long-term geodetic signal at Okmok and the source of the initial ash, it was not the source of the main July 12 phase of OK08, which we propose was derived from a shallower reservoir, R_s. The main July 12 phase of OK08 consisted of more evolved, uniform and largely aphyric WR compositions with 55–56 wt.% SiO_2, like the average of the free-standing MG in the initial ash, and in equilibrium with the most evolved olivines, $Fo_{71–73}$, (Fig. 5a). Given that this composition is more evolved than the magma erupted in 1997, R_s may represent the resident reservoir beneath Cone D (Larsen et al., 2013). R_s is likely located at 1–2 km depth, as reflected by the common CO_2-and H_2O poor MIs measured in this study (Fig. 8a). These depths are much shallower than the 2–6 km stacked sills identified seismically by Miller et al. (2020) and

Kasatkina et al. (2022), but agree with the sill identified by Xue et al. (2020) in the post-2008 inflation at around 1.4 km (Fig. 8d).

The third reservoir, R_d, represents the source of the deep, mafic (<50 wt.% SiO_2) melt preserved in bubble-bearing MIs from the initial phase of OK08. Some of these MIs extend into the range of "high CaO" MIs (≥ 13 wt.%; Schiano et al., 2000), which have been attributed to localized dissolution-reaction and mixing processes (Danyushevsky et al., 2004). The high CaO MIs could have formed from plagioclase dissolution, as they possess a positive Eu* anomaly that correlates with Al_2O_3 concentration (Fig. 4c). Importantly, the four MIs with the highest CO_2 derive from > 6 km depth and are part of the low SiO_2 MI population. These primitive compositions are not observed in either the 1997 scoria (Zimmer et al. 2010) or the main July 12 phase of OK08 (Larsen et al., 2013), and we propose they originate from a unique reservoir (R_d). Given that some of these MIs are hosted in unzoned crystals, R_d was possibly the source of the dike injection that triggered the eruption. Given the range of Fo contents that host such low SiO_2 melts ($Fo_{79–86}$), the range of saturation pressures (2–15 km, Fig. 8b) and diffusion timescales up to six months (e.g., RH-45, Fig 6b), R_d could reflect polybaric storage of inter-connected lenses of magma. Despite being a unique reservoir, R_d shares the same parentage to the rest of Okmok, as all MIs and MG and WR have overlapping Th/Nb (Fig. 4e).

6.2 Precursory seismicity related to magma ascent

Previous studies emphasize Okmok's shallow magma system, with seismic imaging pointing to depths < 10 km and geodetic inflation depths <3 km. Our new homogenized MI CO_2 measurements point to an important, deeper mid-crustal magma storage region (R_d). Firstly, the two MIs with the highest CO_2 content (RH22 and RH31-2, Fig. 7b and 7c) have saturation pressures of 360 and 409 MPa, which translate to ~13 and ~15 km in depth, respectively. These

depths align closely with the deepest earthquakes in the five-hour precursory seismic swarm, ~15 km (Fig. 8c; Garza-Girón et al., 2023). Secondly, both crystals are unzoned in Fo (Fig. 7a and 7d) and especially for RH-22 (Fo_{86}), which is out of equilibrium with the rims of all zoned olivine ($Fo_{77–82}$), must have resided in the OK08 magma for a maximum of one day (Fig. 7e) – possible within the five-hour seismic swarm. Lastly, RH-22 and RH-31 belong to the low SiO_2 MI population unique to the initial ash (Fig. 3a). The appearance of the deep, primitive MI at the start of the eruption supports a diking event to trigger OK08. At the same time, the shallower reservoirs R_m and R_s were also tapped, evident from melt (the rim glass surrounding olivines from R_m and the free-standing MG from R_s) and olivines (with low-CO_2 and bubble-free MIs from R_s). This reinforces the case for a sudden run-up to OK08 and destabilization of several magma reservoirs.

Our results also indicate for the first time the presence of a CO_2-rich fluid at mid-crustal depths beneath Okmok, which may facilitate dike initiation (via overpressure) and propagation (via a gas-rich dike tip; Maimon et al., 2012), thus providing a mechanism for rapid vertical transport to eruption. A magma ascent rate of 15 km in 5 hours, or 0.8 m/s, is typical of other explosive eruptions (Cassidy et al., 2019). The point of CO_2-saturation has also been implicated as a magma "launching depth," based on the appearance of high-CO_2/S gas weeks before eruption of open-vent volcanoes (Ding et al., 2025). Additionally, the distinct shift in the location of hypocenters from the inter-eruptive to the pre-eruptive period (Power et al., 2019, Garza-Girón et al., 2023; Fig. 1a) also suggests the new arrival of a new mid-crustal (15 km) stress source distinct from the slow and steady source of shallow (3–4 km) geodetic inflation.

6.3 Linking petrological and geophysical events at Okmok

Olivines with both reverse and normal zoning record timescales from weeks to years (using DC07 diffusivities), indicating long-term injection of R_d olivines into into R_m or within R_d (normal

zoning) and movement of magma from R_m to R_s (reverse zoning). However, longer timescales are predominantly recorded in reversely zoned crystals, while normally zoned crystals record shorter timescales (Fig. 9a). This inference from the diffusion clocks agrees with the distribution obtained by imaging the randomly selected olivine population, with P_1 (sharp) consisting of more normally zoned crystals and P_3 (long) including more reversely zoned crystals (Fig. 5b). Importantly, there is a ramp up in the number of zoned olivines towards the eruption. With reference to a population of 52 timescales, an average of 0–2 olivines per month (<4% of the timescales) recording mixing events between 2003 and 2007. This rate increases to 2–3 per month (<6%) in early 2008 and then exponentially increases to 5 and 16 per month (~10% and 30%) in the two months before eruption. These timescales provide important context to the evolution towards OK08.

The persistent appearance of reversely zoned crystals supports the hydraulic interconnection of R_m and R_s hypothesized by Walwer et al. (2019) using deformation data and resolved by Miller et al. (2020) and Ohlendorf et al. (2014) using seismic tomography. Apparently, only the liquid from R_m is mixed into R_s as there is a lack of zoned crystals with Fo_{72} rims. The longest reversely-zoned crystal, with a minimum timescale of 3.5 years, indicates that interactions between R_m and R_s were happening well before the shift in the Mogi source 3-4 months prior to eruption (Larsen et al., 2013). The lack olivine timescales coinciding with inflation events prior to 2005 could be related to the loss of resolution of the diffusion clock (Fig. 7b). In further support of Walwer et al. (2019)'s hypothesis that oscillatory deformation is related to magma movement between reservoirs, a portion of reversely zoned crystal timescales (20% n=10) falls within the post-2006 period of oscillatory deformation, consistent with magma from R_m interacting with olivines in R_s (Fig. 9a and 9b).

The increase in early 2008 of the number of mixing timescales per month coincides with the initiation of the last inflation event (Fig. 9e). The subsequent ramp-up in the last two months also coincides with the timing of predicted tensile failure of R_m (Albright et al., 2019) and shift in the Mogi source (estimated to occur in early May; Freymueller and Kaufman (2010; Fig. 9f). The destabilization of R_m could promote more intense mixing, as recorded increase in the number of olivine timescales in the month prior to eruption.

Thus, there are several coincident events recorded in the olivine timescales (using DC07 diffusivities) and sensed geophysically, in the years, months and weeks prior to eruption of OK08. If we instead use the ~10x faster diffusivities from Shea et al. (2023), all the calculated olivine timescales occur 7 months prior to OK08 (SI-17). 45 out of 52 timescales recorded in 43 olivines would indicate magma mixing within 2 months of the eruption. Such results would be consistent with the over-all ramp in events months prior to OK08 (Fig. 9). Use of the Shea et al. diffusivities provide even less resolution in the olivine clocks to events in the years prior to OK08.

6.4 Temporal sequence of events leading up to the eruption

Here we summarize the events preceding OK08, based on combined geochemical and geophysical evidence. During the inter-eruptive period (1997–2008, Fig. 10), Okmok experienced three to four inflation episodes (Fig. 9b) modeled as a single Mogi source at 3.4 km (Lu et al., 2010; Wang et al., 2021); none of these inflation events were accompanied by heightened seismicity (Bennington et al., 2015; Fig. 9d). Aseismic inflation has been attributed in other systems to well-established melt channels feeding the main reservoir (Chouet & Matoza, 2013; White et al., 2011). Concurrently, R_m actively mixes with R_s, evident from reversely zoned crystals, barometry, seismic tomography and oscillatory deformation. R_d also shows mixing

amongst its polybaric storage regions, with one crystal, RH-45 (Fig 6b), containing primitive MI compositions and reflecting magma mixing six months prior to OK08 at ~ 4 km.

In early 2008 (Fig. 10), the renewed inflation and shift in Mogi source coincides with a rapid increase in the number of olivines recording mixing, suggesting more intense magma movement between reservoirs. The possible overlap in timing of tensile failure and shift in the Mogi source, together with the increased number of mixing events could indicate that the system reached a critical state due to an increase in magma supply to a system already "primed" after 11 years of slow and steady inflation. However, we note that in modeling the occurrence of tensile failure during that period, Albright et al. (2019) only consider R_m (and not the connection to R_s) and do not consider the shift in the source identified by Freymueller and Kaufman (2010).

In the five-hours preceding the opening phase of OK08 (Fig. 10), the geophysical behavior beneath Okmok changed to elevated seismicity. Inter-eruptive seismicity has been hypothesized to be caused by reactivation of faults accommodating deformation (Johnson et al., 2010; Fig. 1a), while the pre-eruptive seismicity has been linked to a planar feature opening in the mid-crust (Garza-Girón et al., 2023; Fig. 10), which we have identified to be magmatic (R_d). The rapid formation of the planar structure during the five-hour precursory seismicity links R_d to R_s and R_m, bringing along unzoned crystals from each reservoir (Fo_{72}, $Fo_{77–80}$, Fo_{86}). This small volume of volatile rich magma from R_d may have destabilized the OK08 system and initiated the eruption. While it is also possible that tensile failure of R_m led to depressurization that promoted magma influx from depth, this hypothesis is difficult to test without any deformation data recorded in the months preceding the eruption. There was also no obvious migration of the precursory-seismicity with depth (Garza-Giron et al., 2023).

7. Implications for Eruption Run-Up

Here we have shown that the extremely short run-up for OK08 (5 hours) coincided with rapid ascent of magma from depths comparable to the earthquakes (up to 15 km; Fig. 8a-c). Moreover, the first magma erupted in OK08 was more mafic than the main eruptive phase that followed for 4 hours (Fig. 3a), and contained olivine crystals that host MIs more CO-rich (Fig. 3b) and primitive (Cr-rich; Fig. 4) than any other melts erupted from Okmok caldera over the past 2000 years. The mid-crustal source of crystals implicates a deeper magma storage region beneath Okmok than had been recorded by prior geophysical studies (Fig. 8d). The inferred dike that generated both the precursory seismicity and triggered the eruption forged a new vent in a location 8 km northeast of the vent that had hosted the prior century's eruptions (Fig. 1a). Thus, these observations support a view that the short run-up was a new seismic event that was driven by ascent of a new magma from mid-crustal depths in a new location than prior events, generating the largest eruption at Okmok in over 2000 years. The short run-up of OK08 demonstrates how sudden events may trigger eruptions and motivates the necessity for real-time seismic monitoring that has been embraced by the Alaska Volcano Observatory (Power et al., 2020).

On the other hand, Okmok displayed over a decade of deformation prior to eruption (Fig. 1c), with episodic inflation of shallow magmatic reservoirs (≤ 3 km depth; Fig. 8d) that we have shown were also tapped during OK08 (Figs. 8a, 10). Increasing uplift and approach to tensile failure constitute a different kind of run-up, and one that we also relate to magma input (Fig. 9a-c). With olivine zonation timescales, we document an increase input of magma from deep to shallow storage regions in the months before eruption (Fig. 9e). Apparently, Okmok was already moving toward failure (e.g., it was "primed") when the sudden input of deep, volatile-rich magma triggered eruption. This scenario provides a more sanguine view for forecasting. The success of

455 the Albright et al. (2019) hindcast model for OK08, based entirely on InSAR and GPS data, holds
456 promise for providing warning when inflating systems like Okmok approach failure.

457 Roman and Cashman (2018) present several examples of "top-down" seismic behavior
458 observed at arc volcanoes, whereby shallow precursory seismicity gives way to deeper seismicity
459 that extends to the main magma storage region once the eruption is underway. OK08 represents a
460 counter example of a volcano with "bottom-up" behavior, whereby seismicity deeper than the main
461 magma storage region occurs prior to the eruption. The different depths (Fig. 8a) and short
462 residence time of crystals (Fig. 9e) that we have documented provide compelling evidence that
463 OK08's "bottom-up" precursor was related to the input of deep mafic magma. The causes of "top-
464 down" vs "bottom-up" behavior are as yet unclear. Our study highlights the value of
465 retrospectively integrating petrology with monitoring data to identify magmatic processes
466 underlying precursory signals.

467 Ours is one of a growing number of studies demonstrating that arc magmas are richer in
468 CO_2 than previously thought (>1000s ppm; Ding et al., 2025; Rasmussen et al., 2020; Taracsák et
469 al., 2023). CO_2 exsolution has been proposed to drive high decompression rates, resulting in
470 explosive eruptions (Allison et al., 2021; Barth et al., 2024; DeVitre et al., 2023). The first four
471 hours of OK08 erupted an estimated 0.048 km^3 volume of magma (Unema et al., 2016),
472 corresponding to an approximate mass eruption rate of ~10^7 kg/s and a decompression rate of 10
473 m/s – similar to those at Fuego 1974 and Etna Fall Stratified, other VEI 4 mafic eruptions (Barth
474 et al., 2019, 2024). Thus, OK08 is consistent with the emerging view that decompression rate, and
475 not water concentration, scales with the intensity and magnitude of mafic eruptions (Ferguson et
476 al., 2016; Moussallam et al., 2019). The rapid ascent of magma and the high CO_2 in OK08 MIs
477 (>1800 ppm) suggest that the "launching" depth (Ding et al., 2025), where CO_2 exsolves, may also

478 be an important for eruption triggering in closed-system volcanoes such as Okmok. This premise
479 calls for a re-examination of decades of MI studies that did not account for CO_2 in the vapor
480 bubble. Future studies may explore the physical relationship between the CO_2 content of magmas
481 and the speed of dike propagation; such a relationship could directly link geochemical, geophysical
482 and eruptive processes that lead to explosive eruptions with short run-up.
483

Figure Captions

Figure 1. a) Map of Okmok caldera using the Digital Elevation Model by Schaefer et al. (2012) and earthquake data from Power et al. (2019). Inter-eruptive seismicity represents events before 12 July 2008 and pre-eruptive seismicity represents events on 12 July 2008 before the eruption. Dashed line represents cross section in Figure 10, and is drawn through Cone A (site of 20th century eruptions), Ahmanalix (new cone formed in 2008, near older Cone D). b) A map of Alaska and the Aleutian arc, the red box indicate the location of Okmok. c) Timeseries of volume change of Okmok's magma body since the availability of InSAR data in 1992. Data extracted from Lu et al. (2014), Fournier et al. (2009), Wang et al. (2021), Xue et al. (2020). Post 2008 data for Lu et al. (2014) extracted from National Academies of Sciences, Engineering, and Medicine (2017) report.

Figure 2. a) FTIR spectra of RH22, one of the high CO_2 MIs. Baselines obtained from PyIRoGlass (Shi et al., 2024). b) Transmission microscope image of bubble-bearing MI before and after experimental rehomogenization. Top row is a transmission microscope image of a melt inclusion, MI1, hosted in RH43 and bottom row is a transmission microscope image of a melt inclusion, MI2, hosted in RH31. c) Transmission microscope image of an olivine, RH23, with a doubly-polished (MI1) and two other (MI2 & MI3) rehomogenized MIs.

Figure 3. a) PEC-corrected melt inclusion (MI) and matrix glass (MG) compositions measured in this study from the initial phase of OK08. Untreated MIs that are bubble-free have a black border while bubble-bearing have no border. MG (olivine) represent matrix glass attached to an olivine crystal while MG (free) represent matrix glass picked directly from the ash. Fields are literature data from Larsen et al. (2013). b) H_2O vs CO_2 with isobars calculated from MagmaSat (using composition of RH22, which has the highest CO_2). Samples plotted in the yellow region are below the detection limit of the FTIR. See text and Supplementary Table S1 for detection limits (in all cases < 100 ppm).

Figure 4. Comparison of major and trace element compositions of OK08 melt inclusions and matrix glass from this study to literature whole rock data. Whole rock data from GEOROC, Finney et al., (2008), Larsen et al., (2013). Black solid line represent inferred LLD a) Cr against SiO_2 with labels for the MIs' olivine host Fo content. There is a single data point (arrow) for RH-22 at 394 ppm Cr. b) V against SiO_2. Mixing lines is for the average cluster of MG (Free) and the most primitive homogenized MI. Arrows indicating the inferred liquid line of descent and 'kink' after magnetite starts to crystallize. c) Eu/Eu* against Al_2O_3. Positive Eu anomaly where Eu/Eu* > 1 for whole rocks suggest plagioclase accumulation while for melt inclusions suggest plagioclase dissolution. Negative Eu anomaly where Eu/Eu* < 1 for whole rock suggest plagioclase removal while for melt inclusions suggest plagioclase crystallization. d) Sc against SiO_2 e) Th against Nb

Figure 5. a) Histogram of olivine Fo compositions for initial ash of OK08. Symbols on top represent the glass and whole rock equilibrium Fo content, assuming $Fe^{3+}/Fe^{T} = 0.2$ and $K_D = 0.3$ (symbols the same as Figure 3 and 4). The 1958, 1997, 2008 main phase and 2008 initial ash whole rock data, purple, white, yellow and blue stars respectively, are obtained from this study, Finney et al. (2008), Larsen et al. (2013) and Zimmer et al. (2010). b) Populations derived from backscatter electron profiles for 72 different olivines from 300 – 1mm in size. See text for the description of the different populations. c) Ponytail plot of the zonation profiles modelled for diffusion timescales in this study. The colors represents the timescales modelled using the expression for Fe-Mg diffussion in olivine from Dohmen and Chakraborty (2008).

Figure 6. Fo and P_2O_5 profiles of three representative olivines (a: DF05, b: RH45, c: DF07) with increasing diffusion timescales from a) weeks to b) months to c) years. BSE images on the right show orientations and profiles (red lines). The similar lengthscale for a) and b) olivines but an order of magnitude difference in time is due to the orientation of the profile. a) is almost parallel to the c-axis [001] which has diffusivities 6x faster than the other two axes. Red solid lines represent fit to homogenous initial conditions while blue solid lines represent fit to an initial step profile. Initial conditions are shown as dashed lines, for red and blue models, respectively. t_{DC} represents timescale using diffusivities by Dohmen and Chakraborty (2008) while t_S represents timescale using diffusivities 10x higher as estimated by Shea et al. (2023).

Figure 7. Images, profiles and models of olivines with the highest CO_2 MIs. a) Backscatter electron image of RH31. Transmitted image of b) RH22 and c) RH31. d) Fo profiles of RH22 and RH31 as indicated with colored lines in b) and c). e) Results from a forward 1-D finite difference diffusion model, with profiles along [100] dashed and [100] solid, in order to estimate the time to observe no Fo zoning on the EPMA (assuming no resolution ≤ 5 microns from the rim). f) Results from a forward 3-D finite difference model of crystal sizes 500 μm (dashed) and 1 mm (solid). The 1-D profile is obtained using a [100]-[001] slice through the core of the crystal along [001] axis. A 500 μm initially homogenous crystal at Fo_{72} will equilibrate its core composition with Fo_{80} in 5-11 years at T of 1115°C.

Figure 8. a) Melt inclusion and matrix glass data from this study for OK08 and Zimmer et al. (2010) for the 1997 eruption. Symbols follow previous figures. The estimated depth of the evolved reservoir is represented by the yellow star, using the SiO_2 concentrqation and equilibrium Fo of the 2008 (main) whole rock. Arrow is drawn to guide the eye when comparing the range of depths vs. composition of melt inclusions. a) SiO_2 of olivine hosted MIs and b) Fo content of their olivine host plotted at their MIs vapor saturation depth. c) Earthquakes (EQs) binned by 1 km (Garza-Giron et al. (2023) five-hours pre-eruptive seismicity). d) Compilation of storage regions identified using seismic (red) and geodetic data (green). Data from Mann et al. (2002), Lu et al. (2010), Lu and Dzurisin (2010), Xue et al. (2020), Miller et al. (2020), Kasatkina et al. (2022), Ohlendorf et al. (2014). Description for Miller et al. (2020) and Kasatkina et al. (2022) are as given in those respective studies.

Figure 9. A comparison between various temporal geophysical and geochemical data in the five years prior to the 2008 eruption of Okmok. Blue region represents deflation, red represents inflation and grey represents the shift in the Mogi source observed by Freymueller and Kaufmann (2010) and during the time period with limited GPS data. a) Rank order plot of diffusion timescales (symbols), using diffusivities in Dohmen and Chakraborty (2008). Colors are same as Figure 5. S represent the diffusion timescales of inner shoulder profiles. Unzoned profiles are placed at time 0 with an error of 1 day. Normally zoned profiles are shown in filled symbols, reversely zoned profiles are open. Histograms plot number of olivine timescales/month in the 52 sample population. b) Deformation data from two GPS stations in the caldera (see Figure 1 for locations). Scale is relative to the first data point. OKCD data from Nevada Geodetic Lab (NGL); OKCE from Alaska Volcano Observatory. c) The mean tensile stress and 2σ from joint inversion in Albright et al. (2019). The red line represents 0 MPa tensile strength which is the lowest threshold in Albright et al. (2019). d) Earthquake data using the Power et al. (2019) catalogue. Inter-eruptive and pre-eruptive classification follows Figure 1. e) and f) show data from a year before OK08. e) is a zoomed-in version of a). Arrows shows the ramp up in the number of mixing events recorded in olivines per month. f) is a zoomed-in version of b) and c) replotted together. Arrows indicate notable geodetic events. The uncertainty of the timing of the shift in Mogi source is indicated by the range of arrows (due to a lack of GPS data in May 2008).

585 Figure 10. A model of processes occurring beneath Okmok from the 1997 to the 2008 eruption.
586 The cross-section is SW-NE across the caldera (See dotted line in Fig 1.). Key geochemical and
587 geophysical observations for each time period are emphasized. SiO_2 content of the melt and Fo of
588 the olivine are scaled by intensity of red and green respectively to show the diverse compositions
589 in OK08, and where they are likely placed in the entire plumbing architecture. Stars represent
590 seismicity during the period.
591

References

Albright, J. A., Gregg, P. M., Lu, Z., & Freymueller, J. T. (2019). Hindcasting Magma Reservoir Stability Preceding the 2008 Eruption of Okmok, Alaska. *Geophysical Research Letters*, *46*(15), 8801–8808. https://doi.org/10.1029/2019GL083395

Allison, C. M., Roggensack, K., & Clarke, A. B. (2021). Highly explosive basaltic eruptions driven by CO2 exsolution. *Nature Communications*, *12*(1), Article 1. https://doi.org/10.1038/s41467-020-20354-2

Andrys, J. (2023). Water and oxygen fugacity in subduction zone magmatism. *Open Access Dissertations*. https://doi.org/10.23860/diss-andrys-janine-2023

Barth, A., Newcombe, M., Plank, T., Gonnermann, H., Hajimirza, S., Soto, G. J., Saballos, A., & Hauri, E. (2019). Magma decompression rate correlates with explosivity at basaltic volcanoes—Constraints from water diffusion in olivine. *Journal of Volcanology and Geothermal Research*, *387*, 106664. https://doi.org/10.1016/j.jvolgeores.2019.106664

Barth, A., Portnyagin, M., Mironov, N., Holtz, F., Moussallam, Y., Rose-Koga, E. F., Rasmussen, D., Towbin, H., Gonnermann, H., Mutch, E. J. F., Rotolo, S. G., & Plank, T. (2024). Fast, furious, and gassy: Etna's explosive eruption from the mantle. *Earth and Planetary Science Letters*, *643*, 118864. https://doi.org/10.1016/j.epsl.2024.118864

Bennington, N. L., Haney, M., De Angelis, S., Thurber, C. H., & Freymueller, J. (2015). Monitoring changes in seismic velocity related to an ongoing rapid inflation event at Okmok volcano, Alaska. *Journal of Geophysical Research: Solid Earth*, *120*(8), 5664–5676. https://doi.org/10.1002/2015JB011939

Cassidy, M., Ebmeier, S. K., Helo, C., Watt, S. F. L., Caudron, C., Odell, A., Spaans, K., Kristianto, P., Triastuty, H., Gunawan, H., & Castro, J. M. (2019). Explosive Eruptions

With Little Warning: Experimental Petrology and Volcano Monitoring Observations From the 2014 Eruption of Kelud, Indonesia. *Geochemistry, Geophysics, Geosystems*, *20*(8), 4218–4247. https://doi.org/10.1029/2018GC008161

Chouet, B. A., & Matoza, R. S. (2013). A multi-decadal view of seismic methods for detecting precursors of magma movement and eruption. *Journal of Volcanology and Geothermal Research*, *252*, 108–175. https://doi.org/10.1016/j.jvolgeores.2012.11.013

Costa, F., & Dungan, M. (2005). Short time scales of magmatic assimilation from diffusion modeling of multiple elements in olivine. *Geology*, *33*(10), 837–840. https://doi.org/10.1130/G21675.1

Danyushevsky, L. V., Della-Pasqua, F. N., & Sokolov, S. (2000). Re-equilibration of melt inclusions trapped by magnesian olivine phenocrysts from subduction-related magmas: Petrological implications. *Contributions to Mineralogy and Petrology*, *138*(1), 68–83. https://doi.org/10.1007/PL00007664

Danyushevsky, L. V., Leslie, R. A. J., Crawford, A. J., & Durance, P. (2004). Melt Inclusions in Primitive Olivine Phenocrysts: The Role of Localized Reaction Processes in the Origin of Anomalous Compositions. *Journal of Petrology*, *45*(12), 2531–2553. https://doi.org/10.1093/petrology/egh080

DeVitre, C. L., Gazel, E., Ramalho, R. S., Venugopal, S., Steele-MacInnis, M., Hua, J., Allison, C. M., Moore, L. R., Carracedo, J. C., & Monteleone, B. (2023). Oceanic intraplate explosive eruptions fed directly from the mantle. *Proceedings of the National Academy of Sciences*, *120*(33), e2302093120. https://doi.org/10.1073/pnas.2302093120

636 Ding, S., Plank, T., de Moor, J. M., Moussallam, Y., Brounce, M., & Kelly, P. (2025). Volcanic
637 gases reflect magma stalling and launching depths. *Earth and Planetary Science Letters*,
638 *660*, 119349. https://doi.org/10.1016/j.epsl.2025.119349
639 Dohmen, R., & Chakraborty, S. (2007). Fe–Mg diffusion in olivine II: Point defect chemistry,
640 change of diffusion mechanisms and a model for calculation of diffusion coefficients in
641 natural olivine. *Physics and Chemistry of Minerals*, *34*(6), 409–430.
642 https://doi.org/10.1007/s00269-007-0158-6
643 Ferguson, D. J., Gonnermann, H. M., Ruprecht, P., Plank, T., Hauri, E. H., Houghton, B. F., &
644 Swanson, D. A. (2016). Magma decompression rates during explosive eruptions of
645 Kīlauea volcano, Hawaii, recorded by melt embayments. *Bulletin of Volcanology*, *78*(10),
646 71. https://doi.org/10.1007/s00445-016-1064-x
647 Finney, B., Turner, S., Hawkesworth, C., Larsen, J., Nye, C., George, R., Bindeman, I., &
648 Eichelberger, J. (2008). Magmatic Differentiation at an Island-arc Caldera: Okmok
649 Volcano, Aleutian Islands, Alaska. *Journal of Petrology*, *49*(5), 857–884.
650 https://doi.org/10.1093/petrology/egn008
651 Fournier, T., Freymueller, J., & Cervelli, P. (2009). Tracking magma volume recovery at Okmok
652 volcano using GPS and an unscented Kalman filter. *Journal of Geophysical Research:*
653 *Solid Earth*, *114*(B2). https://doi.org/10.1029/2008JB005837
654 Freymueller, J. T., & Kaufman, A. M. (2010). Changes in the magma system during the 2008
655 eruption of Okmok volcano, Alaska, based on GPS measurements. *Journal of*
656 *Geophysical Research: Solid Earth*, *115*(B12). https://doi.org/10.1029/2010JB007716
657 Garza-Girón, R., Brodsky, E. E., Spica, Z. J., Haney, M. M., & Webley, P. W. (2023).
658 Earthquakes Record Cycles of Opening and Closing in the Enhanced Seismic Catalog of

659 the 2008 Okmok Volcano, Alaska, Eruption. *Journal of Geophysical Research: Solid*
660 *Earth*, *128*(7), e2023JB026893. https://doi.org/10.1029/2023JB026893
661 Ghiorso, M. S., & Gualda, G. A. R. (2015). An H2O–CO2 mixed fluid saturation model
662 compatible with rhyolite-MELTS. *Contributions to Mineralogy and Petrology*, *169*(6),
663 53. https://doi.org/10.1007/s00410-015-1141-8
664 Hartley, M. E., Maclennan, J., Edmonds, M., & Thordarson, T. (2014). Reconstructing the deep
665 CO2 degassing behaviour of large basaltic fissure eruptions. *Earth and Planetary Science*
666 *Letters*, *393*, 120–131. https://doi.org/10.1016/j.epsl.2014.02.031
667 Hélène, B.-B., Georges, B., Thiébaut, d'Augustin, Saskia, E., Etienne, D., & Juliette, V. (2023).
668 Architecture of the Lesser Antilles Arc Illustrated by Melt Inclusions. *Journal of*
669 *Petrology*, *64*(6), egad020. https://doi.org/10.1093/petrology/egad020
670 Hlinka, L., Longpré, M.-A., Pérez, W., Kutterolf, S., & Monteleone, B. (2021). Top–down
671 control on eruptive style at Masaya volcano inferred from melt composition. *Earth and*
672 *Planetary Science Letters*, *572*, 117138. https://doi.org/10.1016/j.epsl.2021.117138
673 Iacovino, K., Matthews, S., Wieser, P. E., Moore, G. M., & Bégué, F. (2021). VESIcal Part I: An
674 Open-Source Thermodynamic Model Engine for Mixed Volatile (H2O-CO2) Solubility
675 in Silicate Melts. *Earth and Space Science*, *8*(11), e2020EA001584.
676 https://doi.org/10.1029/2020EA001584
677 Johnson, J. H., Prejean, S., Savage, M. K., & Townend, J. (2010). Anisotropy, repeating
678 earthquakes, and seismicity associated with the 2008 eruption of Okmok volcano, Alaska.
679 *Journal of Geophysical Research: Solid Earth*, *115*(B9).
680 https://doi.org/10.1029/2009JB006991

Kahl, M., Mutch, E. J. F., Maclennan, J., Morgan, D. J., Couperthwaite, F., Bali, E., Thordarson, T., Guðfinnsson, G. H., Walshaw, R., Buisman, I., Buhre, S., van der Meer, Q. H. A., Caracciolo, A., Marshall, E. W., Rasmussen, M. B., Gallagher, C. R., Moreland, W. M., Höskuldsson, Á., & Askew, R. A. (2022). Deep magma mobilization years before the 2021 CE Fagradalsfjall eruption, Iceland. *Geology*, *51*(2), 184–188. https://doi.org/10.1130/G50340.1

Kasatkina, E., Koulakov, I., Grapenthin, R., Izbekov, P., Larsen, J. F., Al Arifi, N., & Qaysi, S. I. (2022). Multiple Magma Sources Beneath the Okmok Caldera as Inferred From Local Earthquake Tomography. *Journal of Geophysical Research: Solid Earth*, *127*(10), e2022JB024656. https://doi.org/10.1029/2022JB024656

Larsen, J., Neal, C. A., Schaefer, J. R., Kaufman, M., & Lu, Z. (2015). The 2008 phreatomagmatic eruption of Okmok volcano, Aleutian Islands, Alaska: Chronology, deposits, and landform changes. In *Alaska Division of Geological & Geophysical Surveys Report of Investigation* (No. RI 2015-2). Alaska Division of Geological & Geophysical Surveys. https://doi.org/10.14509/29405

Larsen, J., Neal, C., Webley, P., Freymueller, J., Haney, M., McNutt, S., Schneider, D., Prejean, S., Schaefer, J., & Wessels, R. (2009). Eruption of Alaska Volcano Breaks Historic Pattern. *Eos, Transactions American Geophysical Union*, *90*(20), 173–174. https://doi.org/10.1029/2009EO200001

Larsen, J., Śliwiński, M. G., Nye, C., Cameron, C., & Schaefer, J. R. (2013). The 2008 eruption of Okmok Volcano, Alaska: Petrological and geochemical constraints on the subsurface magma plumbing system. *Journal of Volcanology and Geothermal Research*, *264*, 85–106. https://doi.org/10.1016/j.jvolgeores.2013.07.003

Lu, Z., & Dzurisin, D. (2010). Ground surface deformation patterns, magma supply, and magma storage at Okmok volcano, Alaska, from InSAR analysis: 2. Coeruptive deflation, July–August 2008. *Journal of Geophysical Research: Solid Earth*, *115*(B5). https://doi.org/10.1029/2009JB006970

Lu, Z., Dzurisin, D., Biggs, J., Wicks Jr., C., & McNutt, S. (2010). Ground surface deformation patterns, magma supply, and magma storage at Okmok volcano, Alaska, from InSAR analysis: 1. Intereruption deformation, 1997–2008. *Journal of Geophysical Research: Solid Earth*, *115*(B5). https://doi.org/10.1029/2009JB006969

Lu, Z., Masterlark, T., & Dzurisin, D. (2005). Interferometric synthetic aperture radar study of Okmok volcano, Alaska, 1992–2003: Magma supply dynamics and postemplacement lava flow deformation. *Journal of Geophysical Research: Solid Earth*, *110*(B2). https://doi.org/10.1029/2004JB003148

Lynn, K. J., Downs, D. T., Trusdell, F. A., Wieser, P. E., Rangel, B., McDade, B., Hotovec-Ellis, A. J., Bennington, N., Anderson, K. R., Ruth, D. C. S., DeVitre, C. L., Ellis, A. P., Nadeau, P. A., Clor, L., Kelly, P., Dotray, P. J., & Chang, J. C. (2024). Triggering the 2022 eruption of Mauna Loa. *Nature Communications*, *15*(1), 9451. https://doi.org/10.1038/s41467-024-52881-7

Lynn, K. J., Garcia, M. O., Shea, T., Costa, F., & Swanson, D. A. (2017). Timescales of mixing and storage for Keanakāko‘i Tephra magmas (1500–1820 C.E.), Kīlauea Volcano, Hawai‘i. *Contributions to Mineralogy and Petrology*, *172*(9), 76. https://doi.org/10.1007/s00410-017-1395-4

Maimon, O., Lyakhovsky, V., Melnik, O., & Navon, O. (2012). The propagation of a dyke driven by gas-saturated magma. *Geophysical Journal International*, *189*(2), 956–966. https://doi.org/10.1111/j.1365-246X.2012.05342.x

McNutt, S. R., & Roman, D. C. (2015). Chapter 59—Volcanic Seismicity. In H. Sigurdsson (Ed.), *The Encyclopedia of Volcanoes (Second Edition)* (pp. 1011–1034). Academic Press. https://doi.org/10.1016/B978-0-12-385938-9.00059-6

Miller, D., Bennington, N., Haney, M., Bedrosian, P., Key, K., Thurber, C., Hart, L., & Ohlendorf, S. (2020). Linking Magma Storage and Ascent to Eruption Volume and Composition at an Arc Caldera. *Geophysical Research Letters*, *47*(14), e2020GL088122. https://doi.org/10.1029/2020GL088122

Milman-Barris, M. S., Beckett, J. R., Baker, M. B., Hofmann, A. E., Morgan, Z., Crowley, M. R., Vielzeuf, D., & Stolper, E. (2008). Zoning of phosphorus in igneous olivine. *Contributions to Mineralogy and Petrology*, *155*(6), 739–765. https://doi.org/10.1007/s00410-007-0268-7

Moore, L. R., Gazel, E., Tuohy, R., Lloyd, A. S., Esposito, R., Steele-MacInnis, M., Hauri, E. H., Wallace, P. J., Plank, T., & Bodnar, R. J. (2015). Bubbles matter: An assessment of the contribution of vapor bubbles to melt inclusion volatile budgets†. *American Mineralogist*, *100*(4), 806–823. https://doi.org/10.2138/am-2015-5036

Moussallam, Y., Rose-Koga, E. F., Koga, K. T., Médard, E., Bani, P., Devidal, J.-L., & Tari, D. (2019). Fast ascent rate during the 2017–2018 Plinian eruption of Ambae (Aoba) volcano: A petrological investigation. *Contributions to Mineralogy and Petrology*, *174*(11), 90. https://doi.org/10.1007/s00410-019-1625-z

747 Ohlendorf, S. J., Thurber, C. H., Pesicek, J. D., & Prejean, S. G. (2014). Seismicity and seismic
748 structure at Okmok Volcano, Alaska. *Journal of Volcanology and Geothermal Research*,
749 *278–279*, 103–119. https://doi.org/10.1016/j.jvolgeores.2014.04.002
750 Passarelli, L., & Brodsky, E. E. (2012). The correlation between run-up and repose times of
751 volcanic eruptions. *Geophysical Journal International*, *188*(3), 1025–1045.
752 https://doi.org/10.1111/j.1365-246X.2011.05298.x
753 Peccia, A., Moussallam, Y., Plank, T., DallaSanta, K., Polvani, L., Burgisser, A., Larsen, J., &
754 Schaefer, J. (2023). A New Multi-Method Assessment of Stratospheric Sulfur Load From
755 the Okmok II Caldera-Forming Eruption of 43 BCE. *Geophysical Research Letters*,
756 *50*(21), e2023GL103334. https://doi.org/10.1029/2023GL103334
757 Pesicek, J. D., Wellik, J. J., Prejean, S. G., & Ogburn, S. E. (2018). Prevalence of Seismic Rate
758 Anomalies Preceding Volcanic Eruptions in Alaska. *Frontiers in Earth Science*, *6*.
759 https://doi.org/10.3389/feart.2018.00100
760 Portnyagin, M., Almeev, R., Matveev, S., & Holtz, F. (2008). Experimental evidence for rapid
761 water exchange between melt inclusions in olivine and host magma. *Earth and Planetary*
762 *Science Letters*, *272*(3), 541–552. https://doi.org/10.1016/j.epsl.2008.05.020
763 Power, J., Friberg, P. A., Haney, M. M., Parker, T., Stihler, S. D., & Dixon, J. P. (2019). A
764 unified catalog of earthquake hypocenters and magnitudes at volcanoes in Alaska—1989
765 to 2018. In *Scientific Investigations Report* (Nos 2019–5037). U.S. Geological Survey.
766 https://doi.org/10.3133/sir20195037
767 Power, J., Haney, M. M., Botnick, S. M., Dixon, J. P., Fee, D., Kaufman, A. M., Ketner, D. M.,
768 Lyons, J. J., Parker, T., Paskievitch, J. F., Read, C. W., Searcy, C., Stihler, S. D., Tepp,
769 G., & Wech, A. G. (2020). Goals and Development of the Alaska Volcano Observatory

770 Seismic Network and Application to Forecasting and Detecting Volcanic Eruptions.
771 *Seismological Research Letters*, *91*(2A), 647–659. https://doi.org/10.1785/0220190216
772 Putirka, K. D. (2017). Down the Crater: Where Magmas are Stored and Why They Erupt.
773 *Elements*, *13*(1), 11–16. https://doi.org/10.2113/gselements.13.1.11
774 Rasmussen, D. J., Plank, T. A., Roman, D. C., Power, J. A., Bodnar, R. J., & Hauri, E. H. (2018).
775 When does eruption run-up begin? Multidisciplinary insight from the 1999 eruption of
776 Shishaldin volcano. *Earth and Planetary Science Letters*, *486*, 1–14.
777 https://doi.org/10.1016/j.epsl.2018.01.001
778 Rasmussen, D. J., Plank, T. A., Roman, D. C., & Zimmer, M. M. (2022). Magmatic water
779 content controls the pre-eruptive depth of arc magmas. *Science*, *375*(6585), 1169–1172.
780 https://doi.org/10.1126/science.abm5174
781 Rasmussen, D. J., Plank, T. A., Wallace, P. J., Newcombe, M. E., & Lowenstern, J. B. (2020).
782 Vapor-bubble growth in olivine-hosted melt inclusions. *American Mineralogist*, *105*(12),
783 1898–1919. https://doi.org/10.2138/am-2020-7377
784 Roman, D. C., & Cashman, K. V. (2018). Top–Down Precursory Volcanic Seismicity:
785 Implications for 'Stealth' Magma Ascent and Long-Term Eruption Forecasting. *Frontiers*
786 *in Earth Science*, *6*. https://doi.org/10.3389/feart.2018.00124
787 Schiano, P., Eiler, J. M., Hutcheon, I. D., & Stolper, E. M. (2000). Primitive CaO-rich, silica-
788 undersaturated melts in island arcs: Evidence for the involvement of clinopyroxene-rich
789 lithologies in the petrogenesis of arc magmas. *Geochemistry, Geophysics, Geosystems*,
790 *1*(5). https://doi.org/10.1029/1999GC000032

Shea, T., Costa, F., Krimer, D., & Hammer, J. E. (2015). Accuracy of timescales retrieved from diffusion modeling in olivine: A 3D perspective†. *American Mineralogist*, *100*(10), 2026–2042. https://doi.org/10.2138/am-2015-5163

Shea, T., K. Matzen, A., & J. Mourey, A. (2022). Experimental study of Fe–Mg partitioning and zoning during rapid growth of olivine in Hawaiian tholeiites. *Contributions to Mineralogy and Petrology*, *177*(12), 114. https://doi.org/10.1007/s00410-022-01969-8

Shea, T., Ruth, D., Jollands, M., Ohtaki, K., Ishii, H., & Bradley, J. (2023). The presence of silicate melt may enhance rates of cation diffusion in olivine. *Earth and Planetary Science Letters*, *621*, 118370. https://doi.org/10.1016/j.epsl.2023.118370

Shi, S., Towbin, W. H., Plank, T., Barth, A., Rasmussen, D., Moussallam, Y., Lee, H. J., & Menke, W. (2024). PyIRoGlass: An open-source, Bayesian MCMC algorithm for fitting baselines to FTIR spectra of basaltic-andesitic glasses. *Volcanica*, *7*(2), Article 2. https://doi.org/10.30909/vol.07.02.471501

Smythe, D. J., Wood, B. J., & Kiseeva, E. S. (2017). The S content of silicate melts at sulfide saturation: New experiments and a model incorporating the effects of sulfide composition. *American Mineralogist*, *102*(4), 795–803. https://doi.org/10.2138/am-2017-5800CCBY

Taracsák, Z., Mather, T. A., Ding, S., Plank, T., Brounce, M., Pyle, D. M., Aiuppa, A., & Eimf. (2023). Sulfur from the subducted slab dominates the sulfur budget of the mantle wedge under volcanic arcs. *Earth and Planetary Science Letters*, *602*, 117948. https://doi.org/10.1016/j.epsl.2022.117948

Toplis, M. J. (2005). The thermodynamics of iron and magnesium partitioning between olivine and liquid: Criteria for assessing and predicting equilibrium in natural and experimental

systems. *Contributions to Mineralogy and Petrology*, *149*(1), 22–39. https://doi.org/10.1007/s00410-004-0629-4

Unema, J. A., Ort, M. H., Larsen, J. F., Neal, C. A., & Schaefer, J. R. (2016). Water-magma interaction and plume processes in the 2008 Okmok eruption, Alaska. *GSA Bulletin*, *128*(5–6), 792–806. https://doi.org/10.1130/B31360.1

National Academies of Sciences, Engineering, and Medicine (2017). Volcanic Eruptions and Their Repose, Unrest, Precursors, and Timing. National Academies Press. https://doi.org/10.17226/24650

Walwer, D., Ghil, M., & Calais, E. (2019). Oscillatory nature of the Okmok volcano's deformation. *Earth and Planetary Science Letters*, *506*, 76–86. https://doi.org/10.1016/j.epsl.2018.10.033

Wang, J., Lu, Z., & Gregg, P. M. (2021). Inflation of Okmok Volcano During 2008–2020 From PS Analyses and Source Inversion With Finite Element Models. *Journal of Geophysical Research: Solid Earth*, *126*(10), e2021JB022420. https://doi.org/10.1029/2021JB022420

Wauthier, C., Roman, D. C., & Poland, M. P. (2016). Joint analysis of geodetic and earthquake fault-plane solution data to constrain magmatic sources: A case study from Kīlauea Volcano. *Earth and Planetary Science Letters*, *455*, 38–48. https://doi.org/10.1016/j.epsl.2016.09.011

White, R. S., Drew, J., Martens, H. R., Key, J., Soosalu, H., & Jakobsdóttir, S. S. (2011). Dynamics of dyke intrusion in the mid-crust of Iceland. *Earth and Planetary Science Letters*, *304*(3), 300–312. https://doi.org/10.1016/j.epsl.2011.02.038

Wieser, P. E., Iacovino, K., Matthews, S., Moore, G., & Allison, C. M. (2022). VESIcal: 2. A Critical Approach to Volatile Solubility Modeling Using an Open-Source Python3

Engine. *Earth and Space Science*, *9*(2), e2021EA001932. https://doi.org/10.1029/2021EA001932

Xue, X., Freymueller, J., & Lu, Z. (2020). Modeling the Posteruptive Deformation at Okmok Based on the GPS and InSAR Time Series: Changes in the Shallow Magma Storage System. *Journal of Geophysical Research: Solid Earth*, *125*(2), e2019JB017801. https://doi.org/10.1029/2019JB017801

Zimmer, M. M., Plank, T., Hauri, E. H., Yogodzinski, G. M., Stelling, P., Larsen, J., Singer, B., Jicha, B., Mandeville, C., & Nye, C. J. (2010). The Role of Water in Generating the Calc-alkaline Trend: New Volatile Data for Aleutian Magmas and a New Tholeiitic Index. *Journal of Petrology*, *51*(12), 2411–2444. https://doi.org/10.1093/petrology/egq062

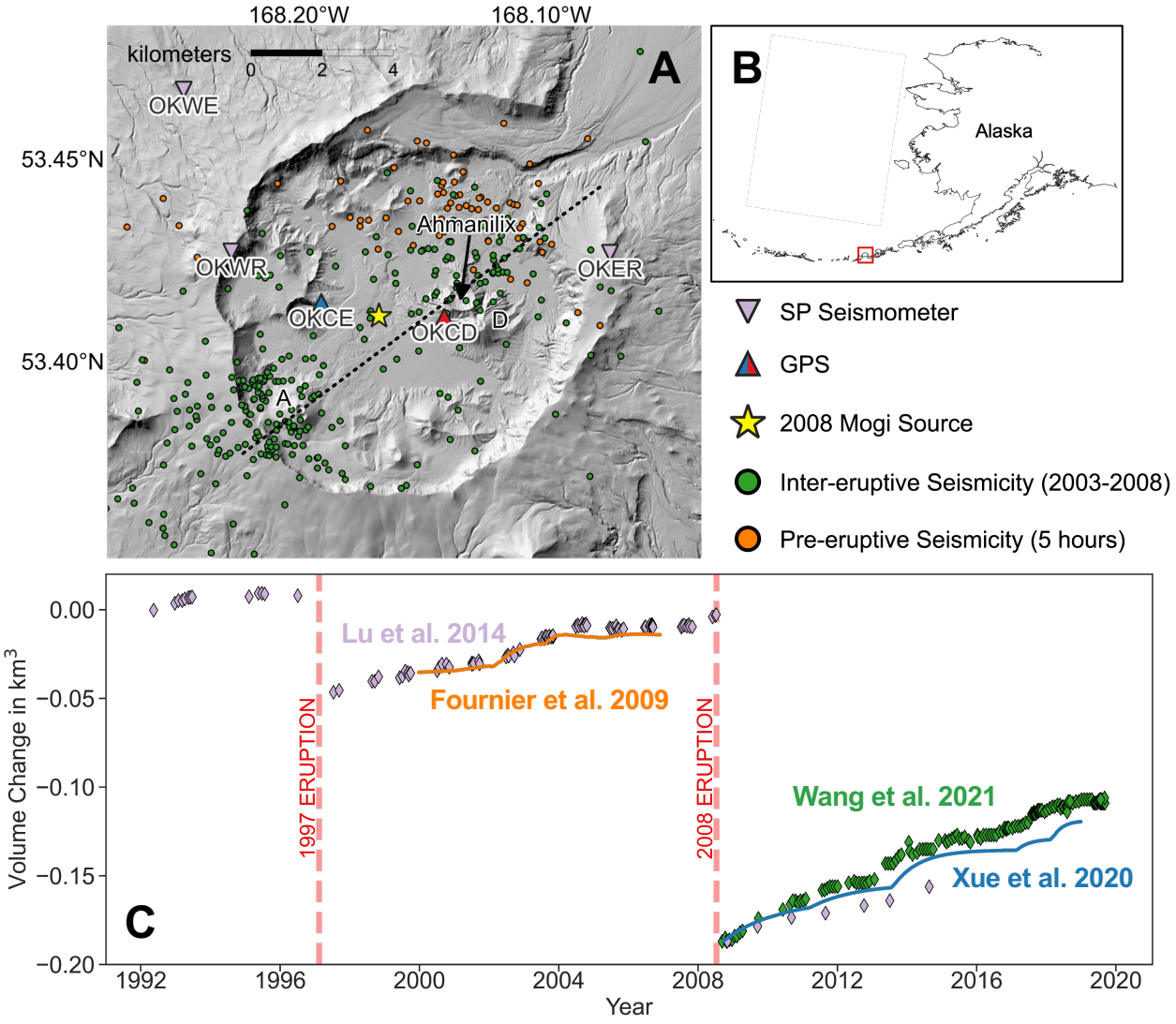

Figure 1. a) Map of Okmok caldera using the Digital Elevation Model by Schaefer et al. (2012) and earthquake data from Power et al. (2019). Inter-eruptive seismicity represents events before 12 July 2008 and pre-eruptive seismicity represents events on 12 July 2008 before the eruption. Dashed line represents cross section in Figure 10, and is drawn through Cone A (site of 20th century eruptions), Ahmanalix (new cone formed in 2008, near older Cone D). b) A map of Alaska and the Aleutian arc, the red box indicate the location of Okmok. c) Timeseries of volume change of Okmok's magma body since the availability of InSAR data in 1992. Data extracted from Lu et al. (2014), Fournier et al. (2009), Wang et al. (2021), Xue et al. (2020). Post 2008 data for Lu et al. (2014) extracted from National Academies of Sciences, Engineering, and Medicine (2017) report.

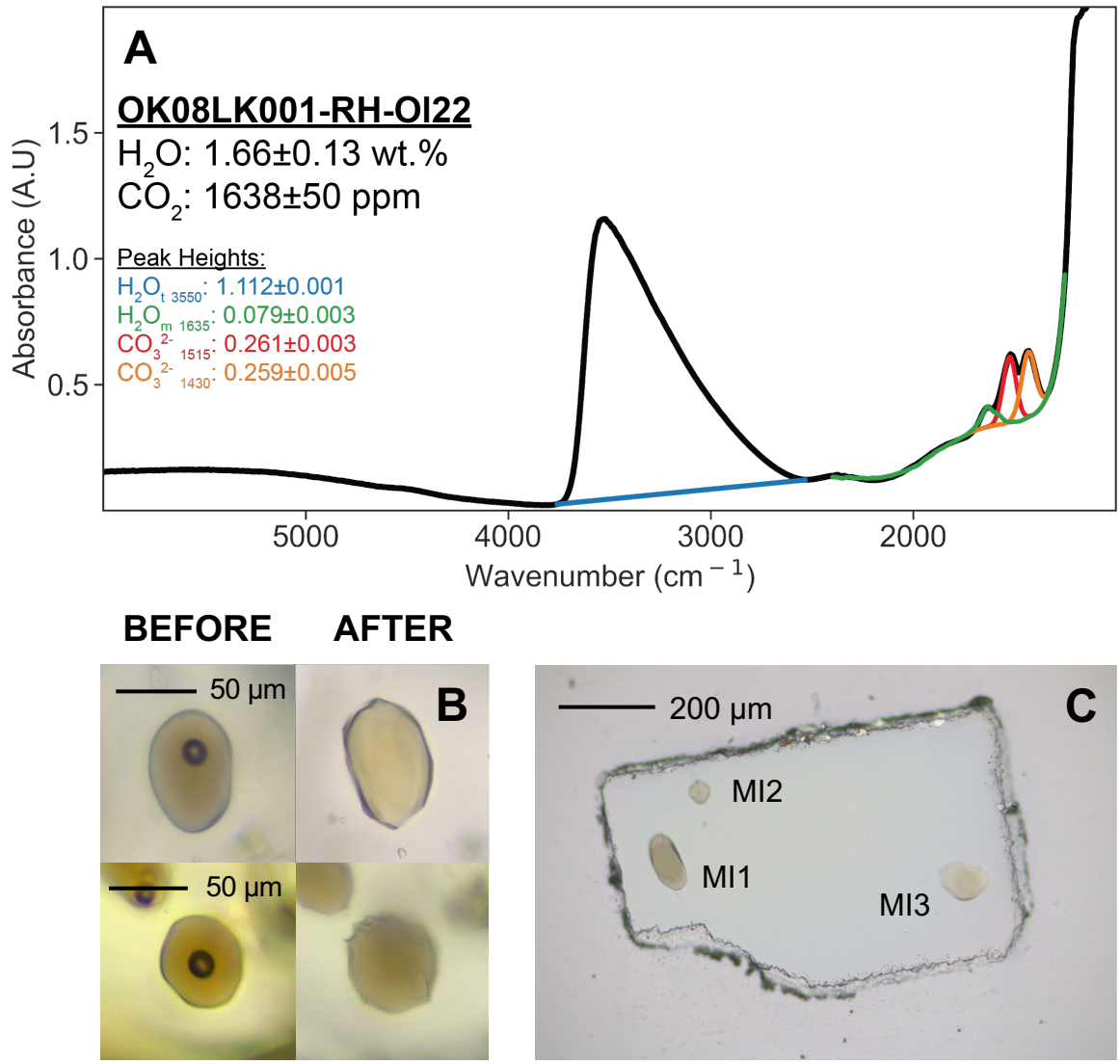

Figure 2. a) FTIR spectra of RH22, one of the high CO_2 MIs. Baselines obtained from PyIRoGlass (Shi et al., 2024). b) Transmission microscope image of bubble-bearing MI before and after experimental rehomogenization. Top row is a transmission microscope image of a melt inclusion, MI1, hosted in RH43 and bottom row is a transmission microscope image of a melt inclusion, MI2, hosted in RH31. c) Transmission microscope image of an olivine, RH23, with a doubly-polished (MI1) and two other (MI2 & MI3) rehomogenized MIs.

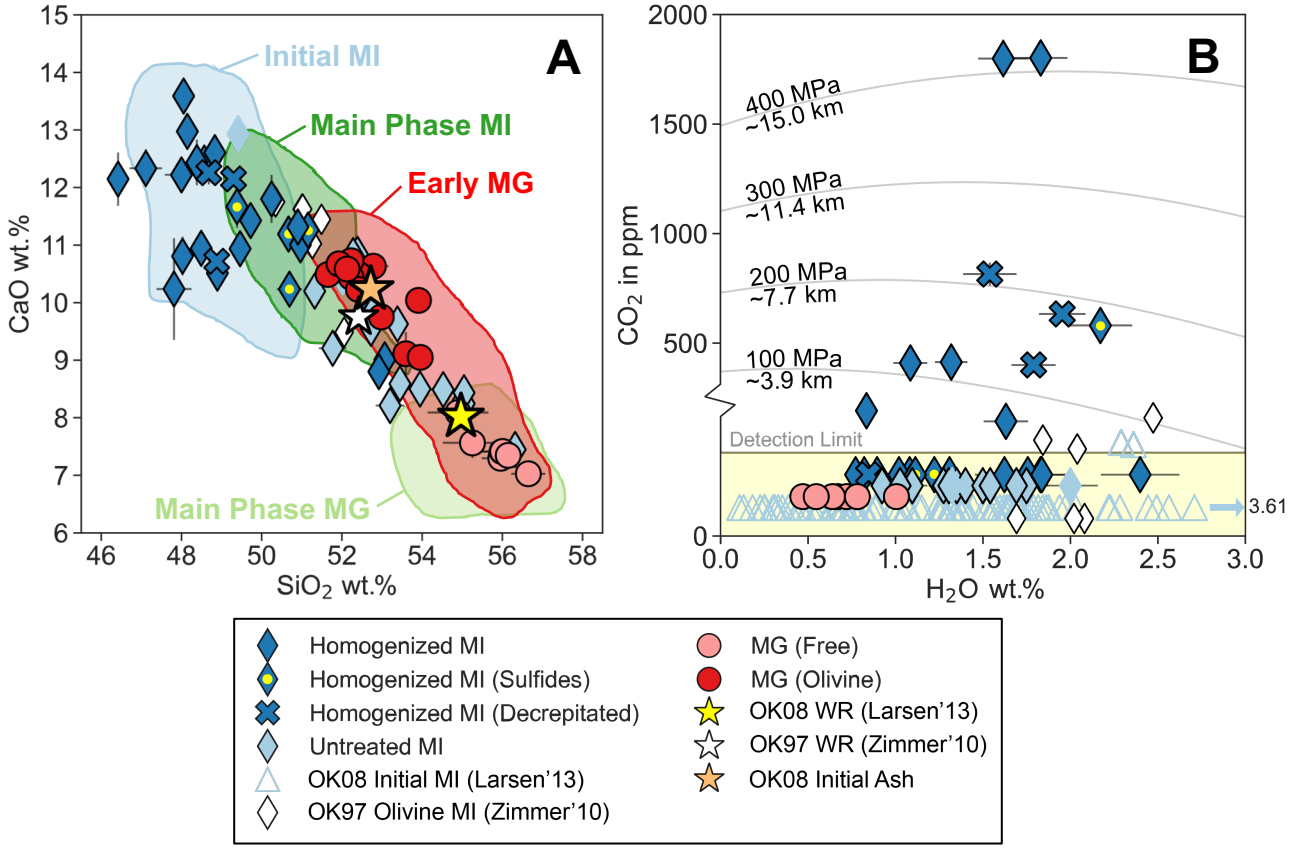

Figure 3. a) PEC-corrected melt inclusion (MI) and matrix glass (MG) compositions measured in this study from the initial phase of OK08. Untreated MIs that are bubble-free have a black border while bubble-bearing have no border. MG (olivine) represent matrix glass attached to an olivine crystal while MG (free) represent matrix glass picked directly from the ash. Fields are literature data from Larsen et al. (2013). b) H_2O vs CO_2 with isobars calculated from MagmaSat (using composition of RH22, which has the highest CO_2). Samples plotted in the yellow region are below the detection limit of the FTIR. See text and Supplementary Table S1 for detection limits (in all cases < 100 ppm).

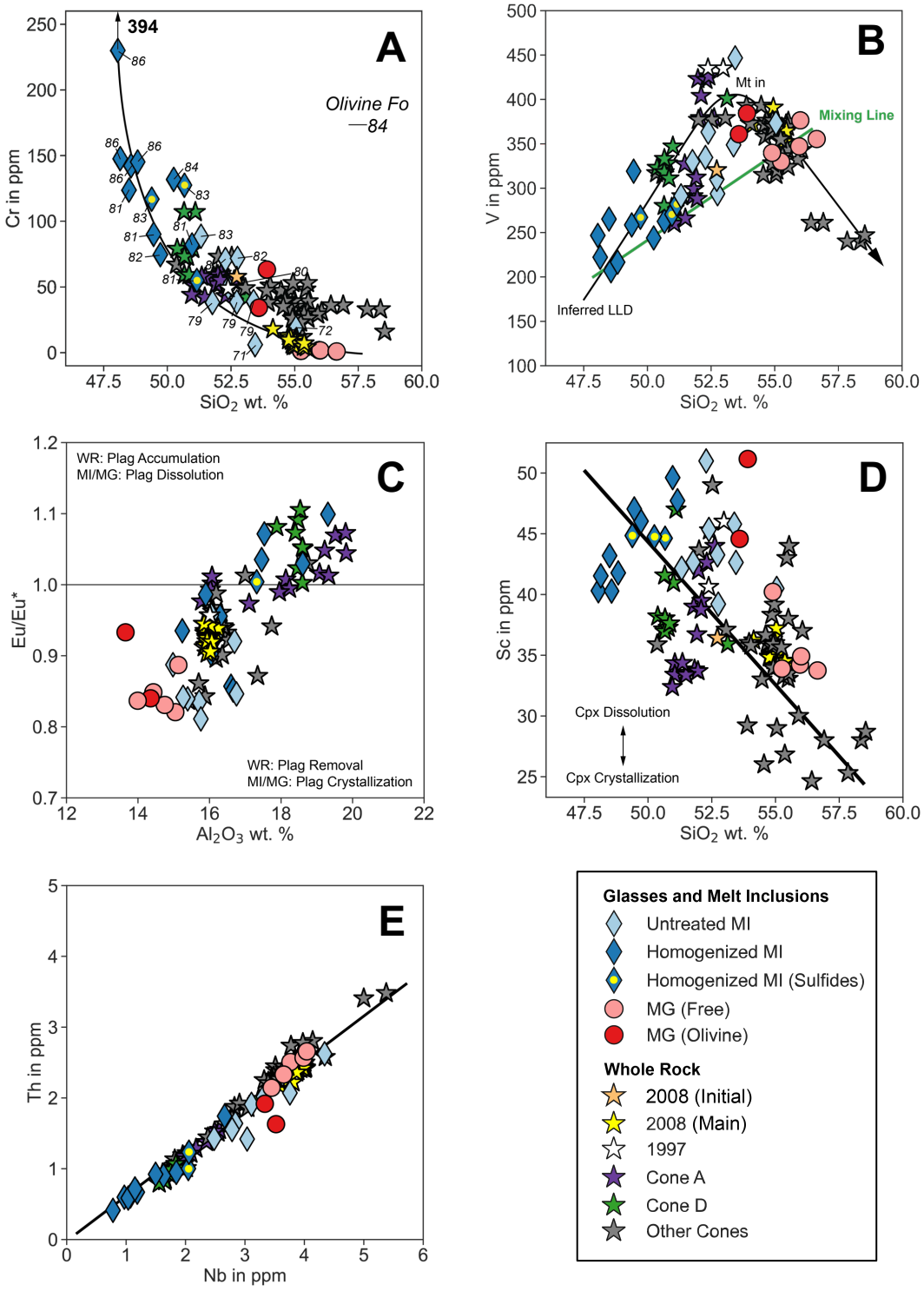

Figure 4. Comparison of major and trace element compositions of OK08 melt inclusions and matrix glass from this study to literature whole rock data. Whole rock data from GEOROC, Finney et al., (2008), Larsen et al., (2013). Black solid line represent inferred LLD a) Cr against SiO_2 with labels for the MIs' olivine host Fo content. There is a single data point (arrow) for RH-22 at 394 ppm Cr. b) V against SiO_2. Mixing lines is for the average cluster of MG (Free) and the most primitive homogenized MI. Arrows indicating the inferred liquid line of descent and 'kink' after magnetite starts to crystallize. c) Eu/Eu* against Al_2O_3. Positive Eu anomaly where Eu/Eu* > 1 for whole rocks suggest plagioclase accumulation while for melt inclusions suggest plagioclase dissolution. Negative Eu anomaly where Eu/Eu* < 1 for whole rock suggest plagioclase removal while for melt inclusions suggest plagioclase crystallization. d) Sc against SiO_2 e) Th against Nb

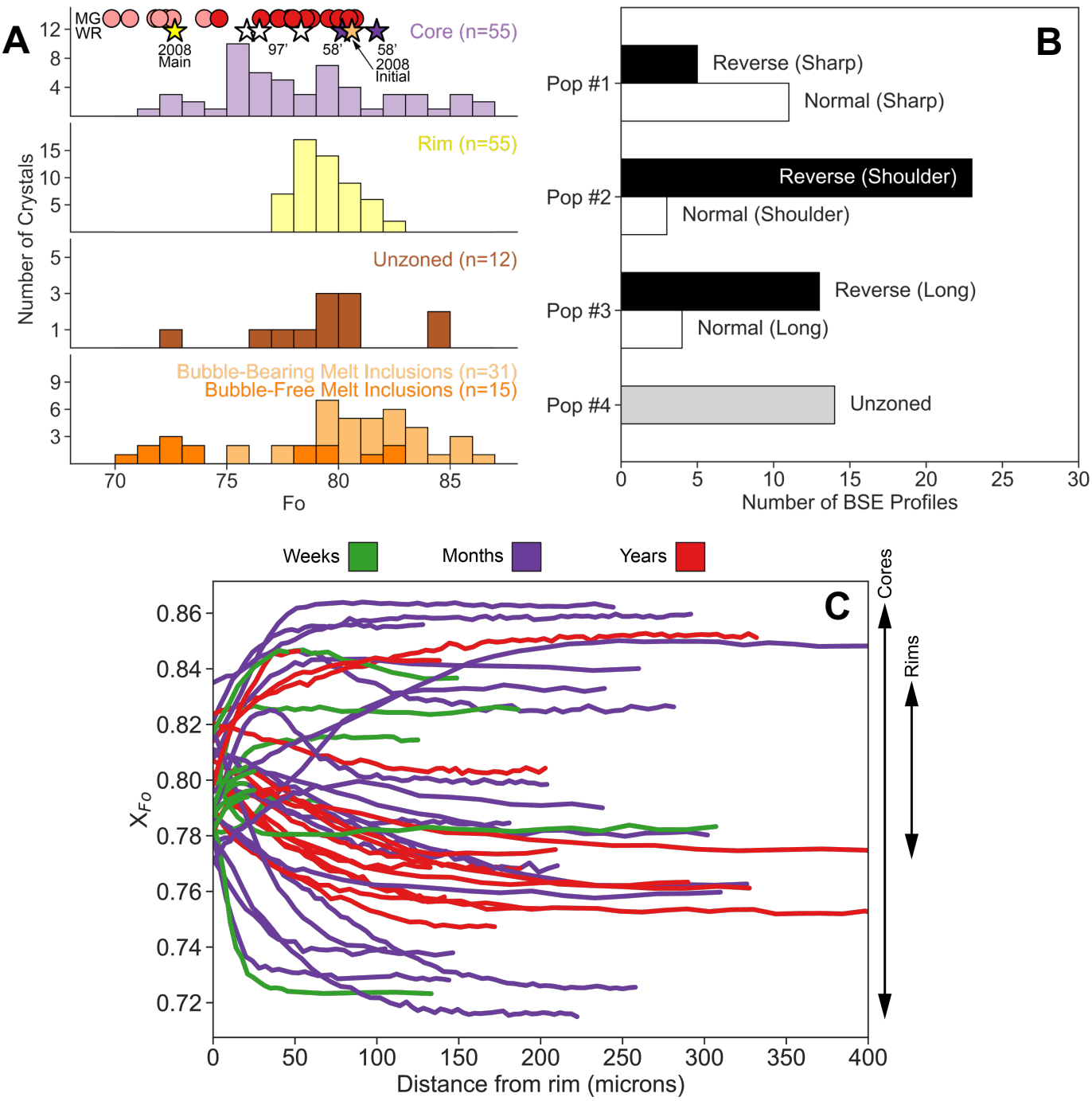

Figure 5. a) Histogram of olivine Fo compositions for initial ash of OK08. Symbols on top represent the glass and whole rock equilibrium Fo content, assuming Fe^{3+}/Fe^{T} = 0.2 and K_D = 0.3 (symbols the same as Figure 3 and 4). The 1958, 1997, 2008 main phase and 2008 initial ash whole rock data, purple, white, yellow and blue stars respectively, are obtained from this study, Finney et al. (2008), Larsen et al. (2013) and Zimmer et al. (2010). b) Populations derived from backscatter electron profiles for 72 different olivines from 300 – 1mm in size. See text for the description of the different populations. c) Ponytail plot of the zonation profiles modelled for diffusion timescales in this study. The colors represents the timescales modelled using the expression for Fe-Mg diffusion in olivine from Dohmen and Chakraborty (2008).

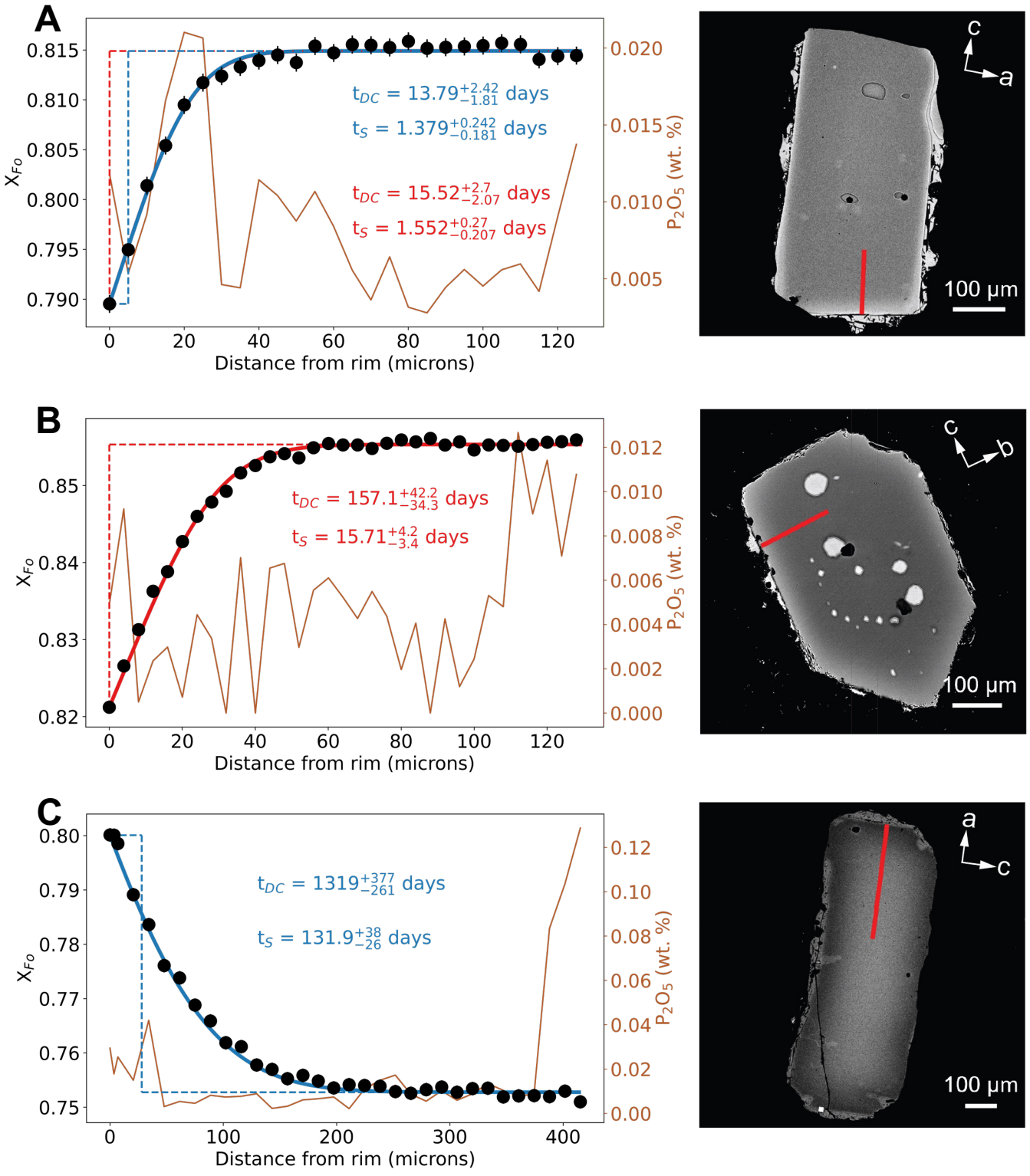

Figure 6. Fo and P_2O_5 profiles of three representative olivines (a: DF05, b: RH45, c: DF07) with increasing diffusion timescales from a) weeks to b) months to c) years. BSE images on the right show orientations and profiles (red lines). The similar lengthscale for a) and b) olivines but an order of magnitude difference in time is due to the orientation of the profile. a) is almost parallel to the c-axis [001] which has diffusivities 6x faster than the other two axes. Red solid lines represent fit to homogenous initial conditions while blue solid lines represent fit to an initial step profile. Initial conditions are shown as dashed lines, for red and blue models, respectively. t_{DC} represents timescale using diffusivities by Dohmen and Chakraborty (2008) while t_S represents timescale using diffusivities 10x higher as estimated by Shea et al. (2023).

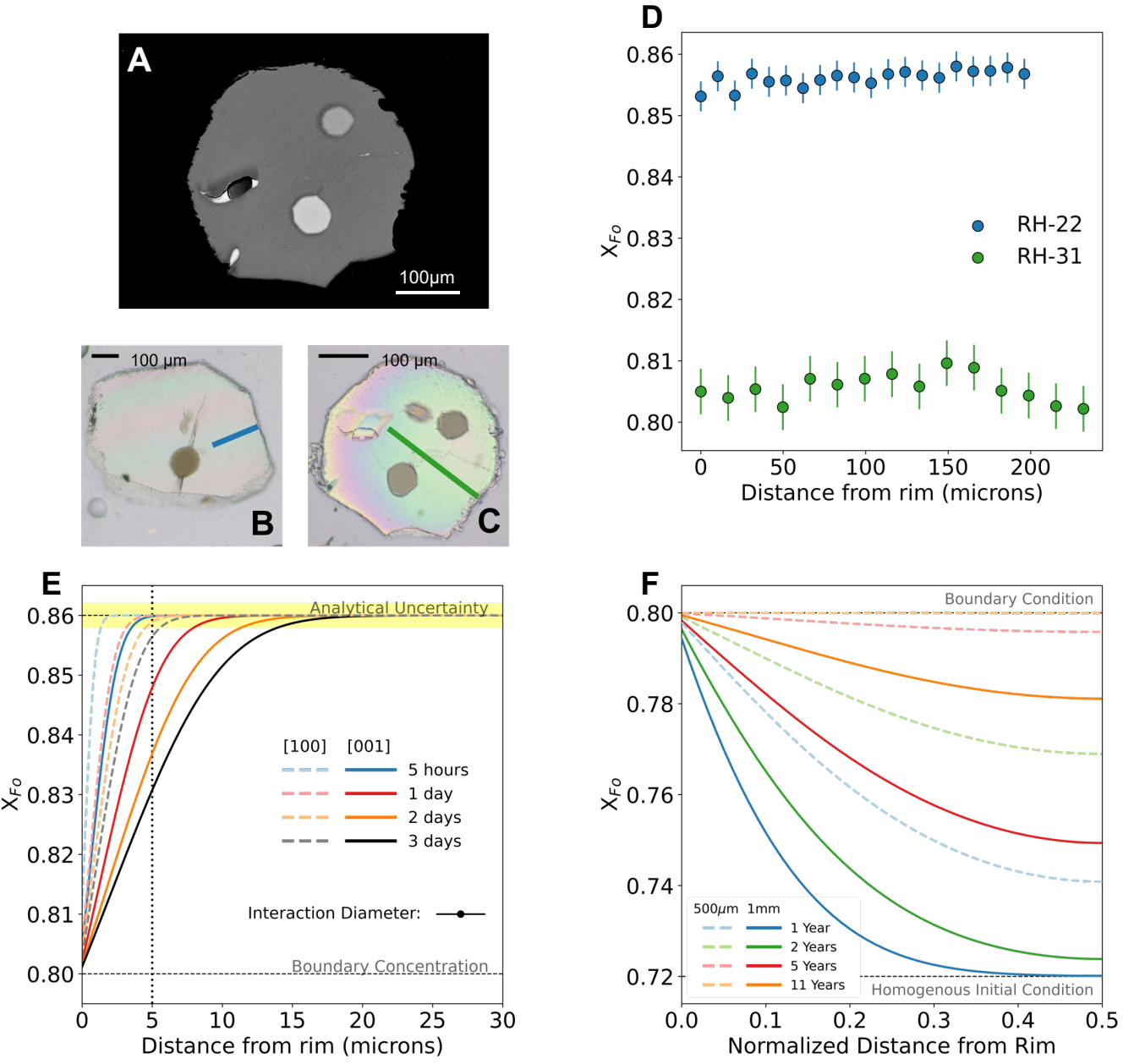

Figure 7. Images, profiles and models of olivines with the highest CO_2 MIs. a) Backscatter electron image of RH31. Transmitted image of b) RH22 and c) RH31. d) Fo profiles of RH22 and RH31 as indicated with colored lines in b) and c). e) Results from a forward 1-D finite difference diffusion model, with profiles along [100] dashed and [100] solid, in order to estimate the time to observe no Fo zoning on the EPMA (assuming no resolution ≤ 5 microns from the rim). f) Results from a forward 3-D finite difference model of crystal sizes 500 µm (dashed) and 1 mm (solid). The 1-D profile is obtained using a [100]-[001] slice through the core of the crystal along [001] axis. A 500 µm initially homogenous crystal at Fo_{72} will equilibrate its core composition with Fo_{80} in 5-11 years at T of 1115°C.

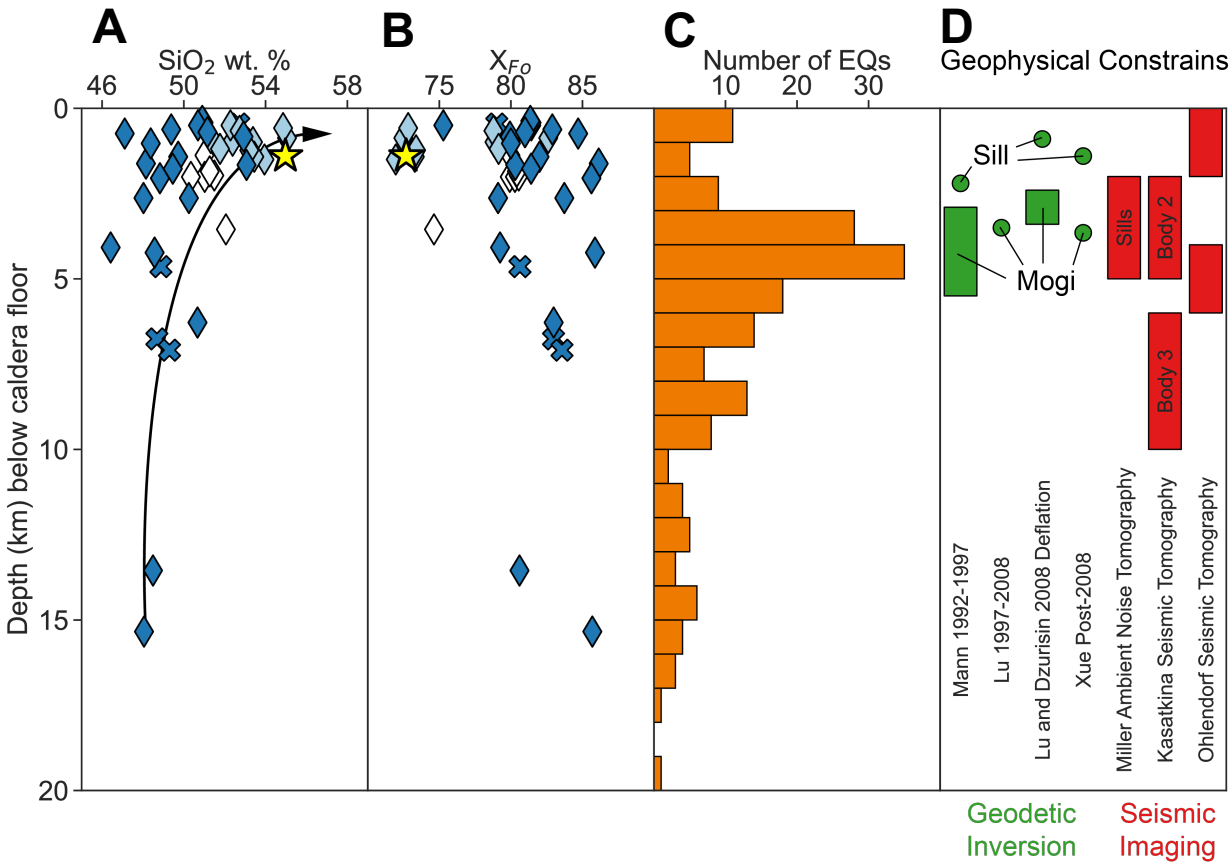

Figure 8. a) Melt inclusion and matrix glass data from this study for OK08 and Zimmer et al. (2010) for the 1997 eruption. Symbols follow previous figures. The estimated depth of the evolved reservoir is represented by the yellow star, using the SiO_2 concentrqation and equilibrium Fo of the 2008 (main) whole rock. Arrow is drawn to guide the eye when comparing the range of depths vs. composition of melt inclusions. a) SiO_2 of olivine hosted MIs and b) Fo content of their olivine host plotted at their MIs vapor saturation depth. c) Earthquakes (EQs) binned by 1 km (Garza-Giron et al. (2023) five-hours pre-eruptive seismicity). d) Compilation of storage regions identified using seismic (red) and geodetic data (green). Data from Mann et al. (2002), Lu et al. (2010), Lu and Dzurisin (2010), Xue et al. (2020), Miller et al. (2020), Kasatkina et al. (2022), Ohlendorf et al. (2014). Description for Miller et al. (2020) and Kasatkina et al. (2022) are as given in those respective studies.

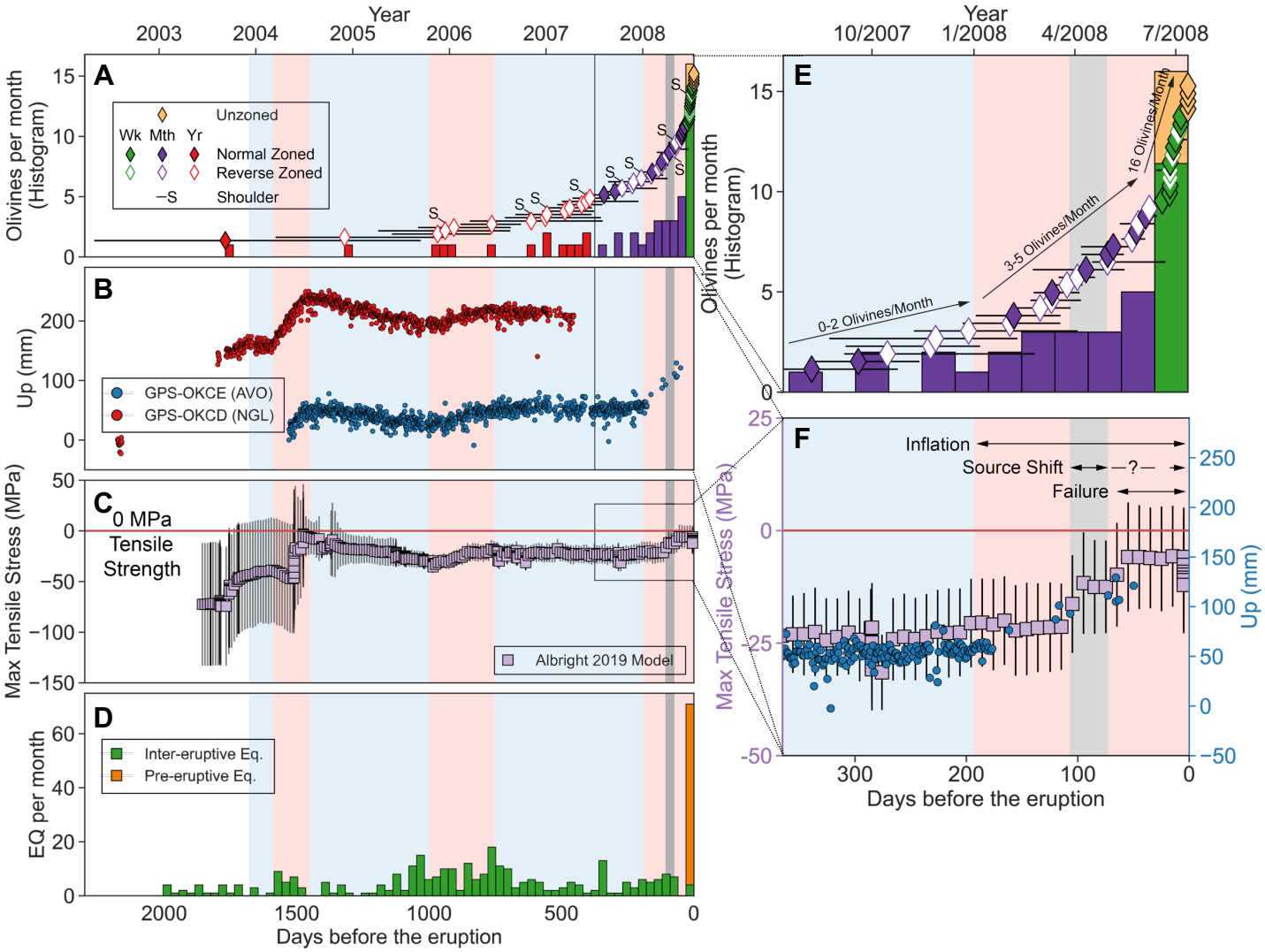

Figure 9. A comparison between various temporal geophysical and geochemical data in the five years prior to the 2008 eruption of Okmok. Blue region represents deflation, red represents inflation and grey represents the shift in the Mogi source observed by Freymueller and Kaufmann (2010) and during the time period with limited GPS data. a) Rank order plot of diffusion timescales (symbols), using diffusivities in Dohmen and Chakraborty (2008). Colors are same as Figure 5. S represent the diffusion timescales of inner shoulder profiles. Unzoned profiles are placed at time 0 with an error of 1 day. Normally zoned profiles are shown in filled symbols, reversely zoned profiles are open. Histograms plot number of olivine timescales/month in the 52 sample population. b) Deformation data from two GPS stations in the caldera (see Figure 1 for locations). Scale is relative to the first data point. OKCD data from Nevada Geodetic Lab (NGL); OKCE from Alaska Volcano Observatory. c) The mean tensile stress and 2σ from joint inversion in Albright et al. (2019). The red line represents 0 MPa tensile strength which is the lowest threshold in Albright et al. (2019). d) Earthquake data using the Power et al. (2019) catalogue. Inter-eruptive and pre-eruptive classification follows Figure 1. e) and f) show data from a year before OK08. e) is a zoomed-in version of a). Arrows shows the ramp up in the number of mixing events recorded in olivines per month. f) is a zoomed-in version of b) and c) replotted together. Arrows indicate notable geodetic events. The uncertainty of the timing of the shift in Mogi source is indicated by the range of arrows (due to a lack of GPS data in May 2008).

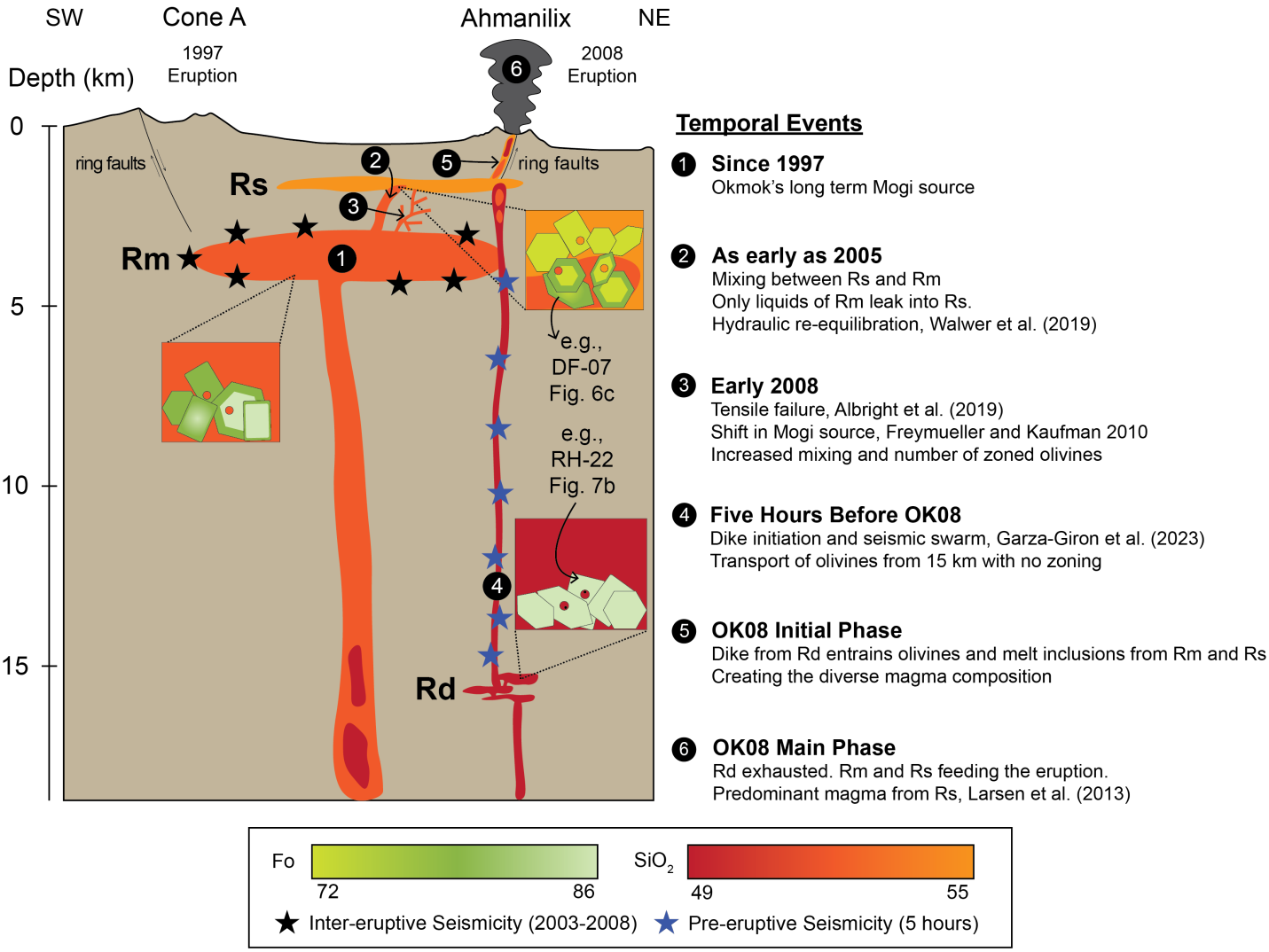

Figure 10. A model of processes occurring beneath Okmok from the 1997 to the 2008 eruption. The cross-section is SW-NE across the caldera (See dotted line in Fig 1.). Key geochemical and geophysical observations for each time period are emphasized. SiO_2 content of the melt and Fo of the olivine are scaled by intensity of red and green respectively to show the diverse compositions in OK08, and where they are likely placed in the entire plumbing architecture. Stars represent seismicity during the period.